A COMPUTATIONAL SPECTRAL IMAGING TECHNIQUE AND ITS APPLICATION IN FORM METROLOGY

by

Nasim Habibi

A dissertation submitted to the faculty of
The University of North Carolina at Charlotte
in partial fulfillment of the requirements
for the degree of Doctor of Philosophy in
Optical Science and Engineering

Charlotte

2017

Approved by:

____
Dr. Faramarz Farahi

____
Dr. Angela Davies

____
Dr. Christopher Evans

____
Dr. Susan Trammell

____
Dr. Kalpathi Subramanian

ABSTRACT

NASIM HABIBI. A computational spectral imaging technique and its application in form metrology. (Under the direction of DR. FARAMARZ FARAHI)

Many existing systems for three-dimensional (3D) shape measurement require mechanical moving parts that limit the measurement speed. A non-contact optical system that does not requires any moving parts can, in principle, increase the speed of measurement. This is particularly an important criterion in volume manufacturing of parts. This motivates us to develop a new optical system for 3D shape measurement with emphasize in the capability of such system to be used as a tool for quality control in volume manufacturing. This dissertation describes the design and implementation of a new 3D shape measurement system. The capability of this system is demonstrated on selected samples with varying slopes. The 3D system presented here is based on a new depth-sensitive, multi-focal imaging system that is developed. This novel imaging system is design by intentionally introducing axial chromatic aberration in the lens system of the camera. A computational unit is also developed to analyze images formed by the designed chromatic lens and calculate the form of a 3D object. The application of this system as a spectral imager is also investigated.

The algorithms implemented in the camera's computational unit as well as the design process of the camera's lens system are described. Simulation and experimental results are provided to evaluate the performance of the spectral imaging camera. The spectral imaging camera has a spectral resolution of 4 nm and spatial resolution of 46 microns. Finally, the experimental results is presented that demonstrate the repeatability of the depth measurements for two measured samples are 11.8 and 10 microns for measurement range of up to 5 mm. These measurements show that the developed system is capable of measuring 3D shape of the object and it is particularly useful if the system is used to measure deviations of parts from the master part used for calibration.

TABLE OF CONTENTS

LIST OF FIGURES

CHAPTER 1 : INTRODUCTION

Metrology techniques can be divided into two broad groups of contact and non-contact techniques. Stylus profilometer and coordinate-measuring machine (CMM) with a tactile probe are examples of contact techniques where a measuring stylus or probe touches the surface of the object. There are numerous non-contact metrology techniques. Interferometry-based techniques [4], focus-based techniques [5], fringe projection [6], triangulation [7], time of flight [8], stereo vision [9], etc., are some examples.

Existing techniques involve scanning at least in one dimension in order to provide the three-dimensional (3D) shape of the object. Mechanical movements limit the speed of measurement and the range of objects that these techniques can be applied to. They are also, in some cases, source of noise and instability. Speed of measurement is especially of great importance for quality control in automated manufacturing and assembly processes where metrology is a major contributor to the ability to detect, in real time, the nonconforming parts that have dimensional and geometrical variations outside of the accepted range of tolerances [10]. Metrology tools are used for quantification of feature heights, surface texture, relative angles, radii of curvature, and other metrics that require distance or surface measurements [5]. Due to large number of measurements, the speed of the metrology technique used in such applications is crucial to achievable production rate.

This was the motivation to develop a 3D shape measurement technique that does not require any mechanical scan and thus is suitable for such applications.

The introduced shape measurement technique uses chromatic aberration to eliminate axial scan. The idea of using chromatic aberration to eliminate the vertical mechanical scan is not new and has been employed in chromatic confocal imaging technique [11-14]. Chromatic confocal imaging is a non-contact single-point distance measuring technique that, in contrast to conventional confocal microscopy [15], does not require a vertical scan because it uses chromatic aberration of the objective lens to disperse the light vertically. In a chromatic confocal probe, the objective lens of a confocal microscope is replaced by a dispersive lens and a spectrometer is placed behind the confocal pinhole. The wavelength at which the intensity output of the spectrometer peaks can be related to the height of the object at that point. Although due to chromatic coding, no vertical scan is required, but chromatic confocal imaging is a single-point measurement technique and lateral scan of the probe across the surface of the object is still necessary.

The shape measurement technique introduced in this dissertation does not require any lateral or vertical scan. Similar to chromatic confocal imaging, we make use of chromatic aberration of a lens system to eliminate the vertical scan. For this purpose, we designed and built a highly dispersive lens system. To eliminate the lateral scan, we use active shape from defocus technique. We project a set of parallel stripes on the object at two different wavelengths and capture an image at each wavelength. The 3D shape of the object determines how much the stripes are blurred in the captured images. Additionally, due to dispersion, the lens system has different focal lengths at the two projection wavelengths and the amount of defocus varies between the two captured images. Effectively, by taking advantage of the dispersion of the lens system, we change the focal length of the camera by changing the wavelength of the illumination instead of moving the object or any component of the imaging system. The amount of defocus in the two captured images is used to calculate the depth map of the object. Active shape from defocus, contrary to conventional and chromatic confocal imaging, is an area-measurement technique and therefore does not require a lateral scan to reconstruct the 3D depth map.

In order to develop the above shape measurement technique, first we need to design and build a spectral camera. The lens system of this camera is highly dispersive and its focal length is a strong function of wavelength. Therefore, the location at which the camera forms focused images of the object is also a function of wavelength. We use computational algorithms to find the location of focused image and correlate that with the spectral content of the object. Hence, we have a spectral imaging camera that is capable of calculating spectral images of the object. Then we use this camera for 3D shape measurement.

The rest of this dissertation is structured as follows: Chapter 2 provides an overview of some focused-based techniques that are related to the topics covered in this research. The overview includes confocal imaging, chromatic confocal imaging, passive shape from focus, passive shape from defocus and active shape from focus/defocus. Chapter 3 gives an introduction to spectral imaging, its applications and existing spectral imaging techniques. Chapter 4 introduces our spectral imaging camera that takes advantage of chromatic aberration of a lens system and correlates the location of conjugate focused image with spectral content of the object. Chapter 5 uses the spectral camera described in

Chapter 4 to develop a 3D shape measurement system. In the developed system, a pattern is illuminated on the object at two different wavelengths. The information in the imaged pattern by the spectral camera at these two wavelengths is used to calculate the 3D form of the object. Chapter 6 summarizes and concludes the dissertation.

CHAPTER 2 : LITERATURE REVIEW ON FOCUSED-BASED DEPTH MEASUREMENT TECHNIQUES

This chapter gives a review of some three-dimensional (3D) depth measurement techniques. The overview is not comprehensive and includes only a selected group of techniques that are directly related to the novel spectral imaging and depth measurement techniques introduced in following chapters of this dissertation. Some of the techniques are discussed in this chapter because they will be implemented and utilized in later chapters and some are mentioned because they provide insight to better understand the concepts that will be important to this research.

All the techniques that are discussed here are focus-based techniques. In other words, they use the fact that an optical system forms a focused image of the object at a conjugate image location as a tool to measure the 3D depth of the object. One can categorize focus-based techniques into point-measurement techniques and area-measurement techniques [5]. Point-measurement techniques measure the depth of one point of the object at each measurement and scan across the surface of the object to find the complete 3D map. Here we talk about confocal and chromatic confocal imaging techniques that belong to this category. Area-measurement techniques, on the other hand, measure the depth information of an area at each measurement. Shape from focus and shape from defocus are the area-measurement techniques that are discussed here and will be used extensively in later chapters of this dissertation.

2.1 Point-measurement techniques

Point-measurement techniques measure the depth of one point of the object and build the 3D map point by point. Two point-measurement techniques are discussed here: confocal imaging and chromatic confocal imaging.

2.1.1 Confocal imaging

Figure 2-1 shows the basic scheme of a confocal imaging system. In a conventional wide-field microscope, the source illuminates the whole object. In a confocal imaging system, on the contrary, light from a source (usually a laser) is focused by the objective lens of a confocal microscope. There is a pinhole on the detector side which is labeled as confocal pinhole in Figure 2-1 and acts as a spatial filter. The in-focus spot (solid line in Figure 2-1) will pass through the pinhole with no or minimum loss while all the out-of-focus light coming from other layers of the object (dashed and dotted lines in Figure 2-1) is rejected by the confocal pinhole. Therefore, the intensity of light collected by the detector can be correlated to how much in focus is the spot and hence to the 3D depth of the spot. Restricting the image and rejecting the out-of-focus light through the confocal pinhole is the key to high spatial resolution achieved by confocal systems.

In order to build a 3D image of the object, both lateral (across the surface of the object) and axial (along the optical axis of the objective lens) scans are required. The axial scan is required to find the depth that results in maximum light passing through the confocal pinhole and reaching the detector. The lateral scan is required because confocal microscopes image one point of the object at a time. The focused beam needs to be scanned across the object in order to form a complete 3D image. There are three groups of methods

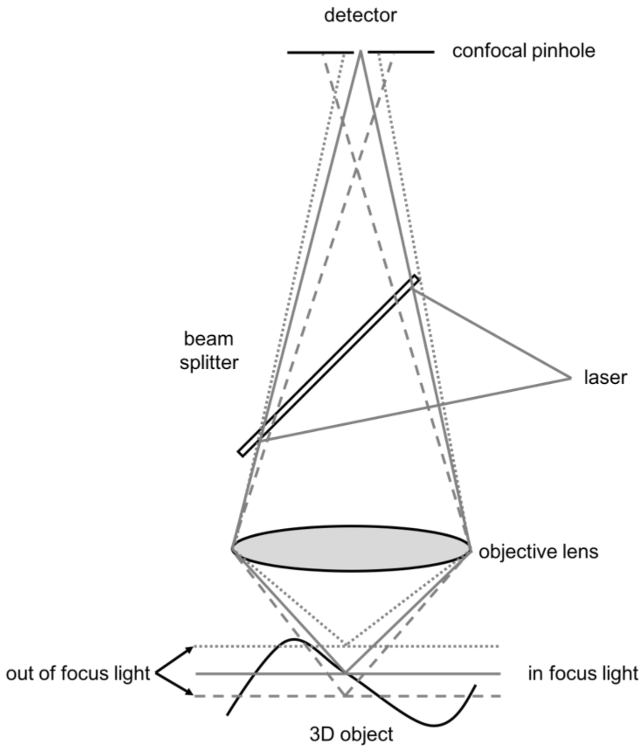

Figure 2-1: Confocal imaging system

to implement the lateral scan [15]: moving the object, moving the source beam and moving the pinhole. In the initial confocal design patented by Minsky in 1957 [16], the object was placed on a moving stage and it was the object that moved and made the scanning possible. Moving the object is simple to implement. Another advantage is that the measurement point remains on-axis with respect to objective lens that makes achieving diffraction-limited performance easier. The drawbacks are that speed of measurement is low and it is difficult to apply to heavy and large objects. Another alternative, which is the most common one, is to move the source beam. This is usually achieved by use of computer-controlled mirrors to guide the beam to desired location on the object. The instruments are more complex but the speed of measurement is higher than moving the object on a stage.

The third option is to use a rotating disc with multiple pinholes to scan the surface of the object. Although we placed confocal imaging in point-measurement category, by using an array of pinholes on a spinning disc, multiple measurements can be done simultaneously. This would greatly improve the speed of measurement. Low light efficiency and high backscatter noise are some of the disadvantages.

The lateral resolution of the confocal system depends on the focused laser spot size on the object. Assuming diffraction limited performance for the objective lens and assuming that two diffraction-limited spots are resolvable when their distance is larger than the first zero of the Airy disk, the lateral resolution of the confocal system is given by [15]:

$$\text{lateral resolution} = 0.61\frac{\lambda}{NA} \tag{2-1}$$

where λ is the wavelength of light and NA is the numerical aperture of the objective lens. The axial resolution, nevertheless, is determined by depth of focus of the objective lens which is the minimum distance that two spots in axial direction can have and still be distinguished as two spots. With the same assumption as above that two spots are distinguishable if the first zero of one of them coincides with the central maximum of the other one, the axial resolution (in object space) of confocal system is given by [15]:

$$\text{axial resolution} = 2n\frac{\lambda}{(NA)^2} \tag{2-2}$$

where n is the refractive index of the object medium and λ and NA are as defined in equation (2-1).

2.1.2 Chromatic confocal imaging

Another focused-based point-measurement technique is chromatic confocal imaging [11-14]. As mentioned above, confocal imaging systems need to scan in both axial and lateral dimensions. Chromatic confocal imaging is an approach to eliminate the axial scan in a confocal system by making use of the chromatic aberration of the objective lens. However, chromatic confocal is still a point-measurement technique and requires a two-dimensional (2D) lateral scan to calculate the 3D depth map.

Figure 2-2 shows a schematic of a chromatic confocal imaging system. Light from a white light source is focused by the objective lens at different distances from the lens as a result of chromatic aberration. There is only one wavelength that is in focus on the surface of the object at the point of measurement; this wavelength is shown as solid green line in Figure 2-2. This specific wavelength is the one that is not rejected by the pinhole on detector side. Therefore, the wavelength that has the maximum transmission through the pinhole can be correlated to the depth of the object. On detector side, there is a grating that gives the intensity of the light as a function of wavelength. The maximum intensity occurs at the wavelength that is in focus on the surface of the object (solid green line in Figure 2-2). Chromatic confocal system does not require axial scan owing to the fact that the lens system focuses different wavelengths at different axial locations and the grating gives the intensity of light in the output of the pinhole as a function of wavelength.

In chromatic confocal system, similar to confocal system, the size of the focused beam on the object determines the lateral resolution calculated by equation (2-1). The axial resolution, on the other hand, is not a function of depth of focus of the objective lens only; it also depends on the spectral resolution of the grating.

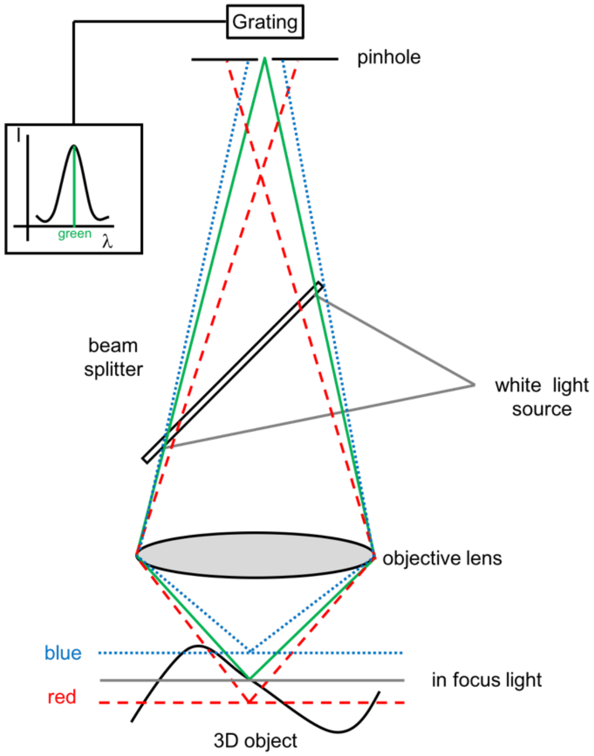

Figure 2-2: Chromatic confocal imaging system

2.2 Area-measurement techniques

Area-measurement techniques, in contrast to point-measurement techniques, measure the depth of an area of the object without a lateral scan. Shape from focus and shape from defocus are two focus-based area-measurement techniques that are discussed here. These two are also implemented in our spectral imaging technique introduced in Chapter 4 and depth measurement technique introduced in Chapter 5.

We divided the shape from focus and shape from defocus techniques into passive and active groups. Active techniques require projecting some kind of pattern on the object; whereas, passive techniques measure the 3D depth map without any active light projection. The issue with passive techniques is that they require the object to have some kind of textures and features in order to be able to measure the level of focus or defocus. If the object lacks natural texture on the surface, active projection of a pattern is required.

Passive shape from focus and defocus techniques use images from a single camera but taken at different focus settings to calculate the depth of the object. Passive stereo techniques, on the other hand, use images from two cameras taken from different angles to calculate the depth. Therefore, shape from focus and defocus techniques have the advantage that they do not have to solve the issue of correspondence between two images as in stereo. In active shape from focus and defocus, the projector and the camera have the same optical axis. Hence, they do not suffer from occlusion and shadowing problems like other active depth measurement techniques where there is an angle between the projector and the camera such as triangulation or structured light based techniques.

2.2.1 Passive shape from focus

Figure 2-3 illustrates how the lens system forms a focused image of point P of the object. The location of focused image is marked as P' in Figure 2-3 and its distance from the lens system is i. Passive shape from focus techniques work based on the fact that if we know the camera parameters and the location of the focused image, P', we can use lens equation to find the depth of the object. The focal length of the camera, f, the depth of point P, o, and the distance of the focused image from the lens system, i, are related by equation (2-3):

$$\frac{1}{\mathrm{f}} = \frac{1}{o} + \frac{1}{i} \tag{2-3}$$

In shape from focus algorithm, the imaging detector is placed at different distances from the lens system and an image is captured at each location. Next, a focus measure

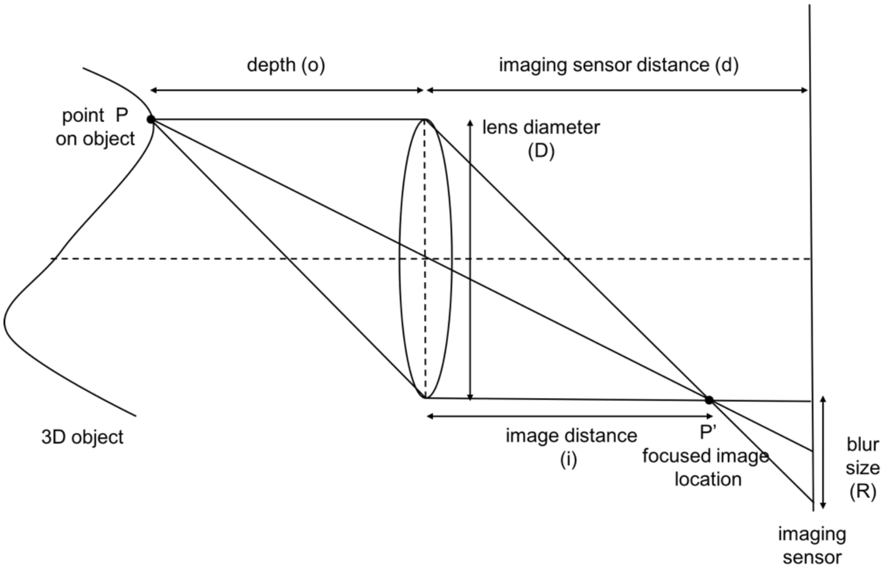

Figure 2-3: A focused image of the point P on the 3D object is formed by the lens system at P'. The location of P' depends on the depth of point P. Shape from focus algorithm searches for the location of P' and uses that to calculate the unknown depth of the point P. The blur size, R, is also a function of the depth of point P. Shape from defocus algorithm determine the blur size on the imaging sensor and uses that to calculate the unknown depth of the point P.

operator is defined that measures the level of focus for each pixel of the image at each location. The location at which the focus measure operator has the maximum value for a pixel, gives the location of focused image (i in equation (2-3)) for that pixel. Subsequently, the depth of that pixel is calculated by equation (2-3).

Determining the level of focus is a critical part of the shape from focus algorithm. Various operators have been proposed in literature to measure the degree of focus for each pixel of each captured image [17]. Some operators are gradient-based [18-21] and work on the assumption that there are sharp edges and features present in the focused image; therefore, the gradient of intensity should be larger for a focused image compared to a blurred one. Another operator to measure the degree of focus is the second derivative or Laplacian of the image [19, 20, 22-25]. High value of second derivative also represents the presence of sharp edges and features. The coefficients of the discrete wavelet transform can be used as a focus measure operator too [26-28]. One can describe the frequency content of the image using these coefficients. A focused image is expected to have larger high frequency content, again because of sharp changes in intensity. Hence, the coefficients of the discrete wavelet transform can be used to measure the level of focus.

Once a sequence of images is captured at different distances from the lens system and degree of focus is measured for all these images, next step is to determine the depth. A widely used technique first proposed in [22], is to fit a Gaussian to the focus measure values of each pixel and choose the location of the maximum of the Gaussian to be the location of focused image for that pixel.

2.2.2 Passive shape from defocus

Passive shape from defocus techniques are based on blurring effect of the imaging system. Instead of searching for the location of focused image like shape from focus, shape from defocus algorithms measure the amount of defocus or blur at the location of imaging sensor. The blur size is shown as R in Figure 2-3. Using lens equation and similar triangles shown in Figure 2-3, the relation between depth of point P, camera parameters and blur size is given by [29]:

$$o = \frac{fd}{d - f \pm R\frac{f}{D}} \tag{2-4}$$

where o is the unknown depth of point P, f is the focal length of the lens, D is the diameter of the lens, d is the distance of the imaging sensor from the lens and R is the blur size. The $\pm$ sign is for the two cases where the imaging sensor is before or after the focused image location. Because of this ambiguity, usually at least two images are required for shape from defocus algorithm. Using more than two images imposes over-constraint to the problem and can improve the result. There are techniques that use only one image [30-32] by estimating the amount of blur at sharp edges in the object. These techniques have difficulty in dealing with above-mentioned ambiguity and are usually used only when no more than one image of the object is available.

The input to shape from defocus algorithm is two images captured with two different sets of camera parameters (focal length of the lens, diameter of the lens and imaging sensor location). Figure 2-4 depicts two captured images, i_1 and i_2, for the case where the imaging sensor location is the parameter that changes between the two captured images. One of the images is focused at the farthest distance within range of measurement and the other one at closest distance. These two images are referred to as far-focused and near-focused images. The algorithm calculates the blur values for these two images at every pixel. The objective of the algorithm is to determine the depth map of the whole object from the calculated blur values.

The defocused images i_1 and i_2 are modeled by convolving the focused image by the point spread function (PSF) of the lens system as follows:

$$\begin{aligned} \mathrm{i}_1(x,y) &= i_f(x,y) * h(x,y;o,c_1) \\ \mathrm{i}_2(x,y) &= i_f(x,y) * h(x,y;o,c_2) \end{aligned} \tag{2-5}$$

where $*$ is the convolution symbol, i_f is the focused image and h is the PSF. o and c represent the unknown depth of the object and the known camera parameters. They are included in equation (2-5) to emphasize that the PSF depends on the depth of the object

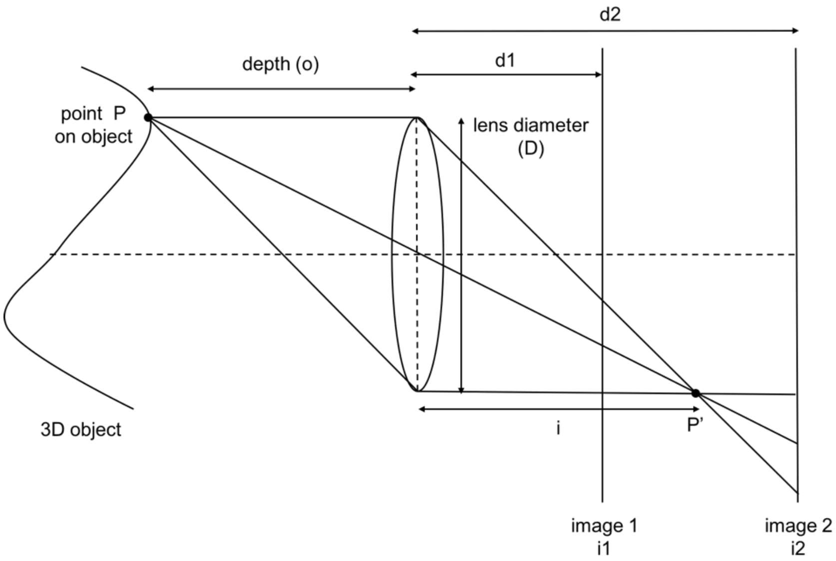

Figure 2-4: Two images of the object are captured at two different distances from the lens system. Shape from defocus algorithm calculates the blur values and use them to reconstruct the 3D depth map of the object.

and the camera setting. In the case shown in Figure 2-4, the variable camera parameters are the locations of the imaging sensor or more specifically the distance between the imaging sensor locations and focused image. Shape from defocus algorithms assume a distribution for the PSF; most common ones are Gaussian and pillbox distributions where the standard deviation of the Gaussian or the radius of the pillbox are functions of o and c. Given two captured images, i_1 and i_2, and the known camera parameters, c_1 and c_2, the objective is to use equation (1-5) and solve for unknown depth of the object, o.

2.2.3 Active shape from focus/defocus

When the object lacks any texture or is weakly textured, passive shape from focus and defocus techniques fail to find the location of focused image or calculate the amount of defocus and hence are not able to measure the depth. In these cases, we need to actively introduce some texture on the object. Active shape from focus/defocus techniques involve projecting a pattern onto the object. The projected pattern gets defocused in the captured images as a function of depth (the third dimension) of the object. Therefore, the captured images from the projected pattern contains information about the 3D map of the object.

Calculating the depth of an object based on the change in spread of a projected pattern was introduced in [33]. The pattern projected on the object is an array of dots or a set of stripes. There is an annular-aperture or a double-aperture mask placed in front of the imaging lens. The size of the dots or stripes is measured on the image. The size is proportional to the distance between the object point and the plane of best focus. The larger is the size of the imaged dot or stipe, the more defocused is object at that point.

Pentland et al. [34] also projected a set of parallel stripes on the object and measured the apparent blurring of the stripes. They measured the energy (integral of intensity squared) of each spread line. Assuming that the lens system spreads a line into a uniform stripe with some radius, the radius is proportional to the energy of the blurred stripe. And the radius of the stripe at each point is proportional to the depth of that point.

Watanabe et al. [35] project a checkerboard pattern on the object. The horizontal and vertical periods of the projected checkerboard pattern were chosen in a way to maximize the response of the focus operator (Laplacian operator) at the frequencies that are used for blur calculation. After projection, two images of the object were captured simultaneously with different focus settings. The contrast map of the two images were computed and compared pixel by pixel to produce a dense depth map.

Ghaita et al. [36], project a sequence of horizontal stripes on the object. A focus operator is introduced, namely simple cell, to measure the blur values locally. The introduced focus operator responds strongly to lines or edges with a specific orientation and spatial frequency and is tuned to the orientation and frequency of the projected pattern. For other texture orientations, the simple cell will respond weakly and this will result in a decreased sensitivity as compared to the Laplacian operator, used for example in [35], when applied to arbitrary object textures.

Zhang and Nayar present a frequency-domain method for estimating the spatially-varying defocus kernel of a projector which is a function of depth and can be used to recover the 3D geometry of the scene [37]. The basic idea is to shift an illumination pattern (set of parallel stripes) with a wide range of frequencies across the scene. As the pattern is shifted, points at different distances to the projector exhibit different amounts of blur in their temporal radiance profile. This temporal blur is used for depth recovery.

Lertrusdachakul et al. used a video projector to project a grid of dots on the object [38]. A stack of images is acquired but three of them are selected for each spot to measure the blur. A 2D Gaussian function is fitted to the dots on selected images. The blur value is proportional to the standard deviation of the fitted 2D Gaussian. The larger is the standard deviation, the higher is the level of blur. The depth is estimated from the blur values. The same group in a later paper repeated the same process with a set of parallel stripes instead of dots [39].

In Chapter 5 of this dissertation, we introduce an active depth measurement technique that includes a dispersive imaging lens system and takes advantage of the dispersion of the lens system for depth measurement. Two illumination patterns at two different wavelengths are projected by a laser projector on the object and an image is captured under each illumination. These two images are blurred differently due to dispersion of the lens system. The difference is used to calculate the depth map of the object.

2.3 Summary

This chapter gives a review of some depth measurement techniques that are related to the research covered in this dissertation. All the discussed techniques are focus-based; in other words, they use the fact that a lens system forms a focused image of the object at a conjugate location to find the 3D depth of an object. Focused-based techniques were divided into point-measurement and area-measurement categories.

Confocal and chromatic confocal imaging system are two point-measurement focused-based techniques. Confocal imaging system requires both lateral and axial scans to calculate the depth map. Chromatic confocal takes advantage of chromatic aberration of the objective lens to eliminate the axial scan in confocal imaging.

Shape from focus and defocus are area-measurement focus-based techniques. They were divided into passive and active groups. Passive shape from focus techniques capture many images of the object at incremental focus settings and search for the location of focused image. Passive shape from defocus techniques use only two images of the object taken at two different focus settings and measure the amount of defocus at these two images. The amount of defocus can then be correlated to depth of the object. Active shape from focus/defocus techniques require projection of an illumination pattern on the object. The image of the projected pattern is blurred as a function of the depth of the 3D map of the object. Therefore, it can be used to reconstruct the depth map of the object.

CHAPTER 3 : LITERATURE REVIEW ON SPECTRAL IMAGING

Spectral imaging (SI) is adding a third dimension to an image by providing the spectral content of each pixel along with its intensity. If imaging is finding the intensity map of a scene in spatial coordinates and spectroscopy is finding the intensity of a light source in spectral coordinates, SI is measuring the intensity as a function of wavelength, λ, for any point (x,y) of the scene. In this sense, SI can be considered as either an extension to imaging by adding the spectrum of each pixel to the data or an extension to spectroscopy by adding two-dimensional spatial maps to the spectral information. Therefore, the output of SI is a three-dimensional data cube which is basically a stack of images each captured at a specific wavelength and gives intensity as a function of both position and wavelength; i.e. $I(x,y,\lambda)$. Figure 3-1 shows this three-dimensional data cube.

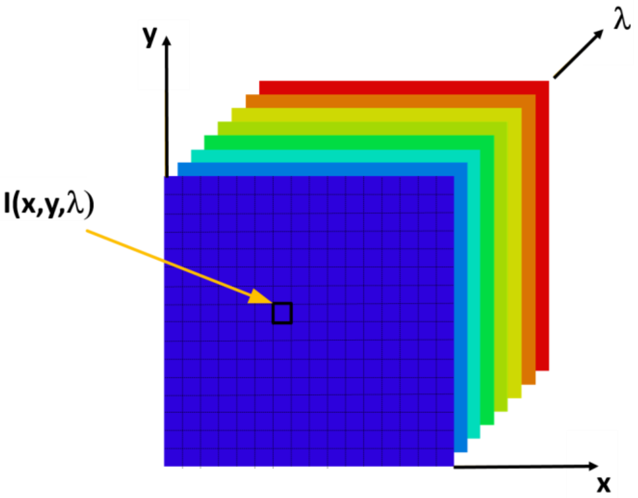

Figure 3-1: The output of SI is a data cube that gives intensity as a function of position and wavelength.

The purpose of this chapter is to introduce SI, its applications and a few current techniques used for SI.

3.1 Spectral imaging applications

SI has found applications in various fields such as remote sensing [40], agriculture and food industry [41], biomedical imaging [42], crime scene inspection [43], archeology and art conservation [44], etc. In this section, some of these applications will be briefly reviewed.

3.1.1 Remote sensing

Remote sensing is the area from which SI first emerged [40]. Remote sensing is the field of extracting information about an object from a distance without physical contact. SI can be a useful tool in this field because each band of the SI data cube provides information about the spectral characteristics of materials in the scene. The spectral data corresponding to each pixel carries information about the chemical composition of the material imaged on that pixel. In remote sensing applications of SI, usually the imager is on an airborne or space-based platform and captures images of the objects on earth. Therefore, the object is far away from the spectral imager. Other aspects of remote sensing are that the scene illumination and environmental condition are unknown and hence there are sources of uncertainty in the problem. Figure 3-2 shows how SI can determine the geological map of various mineral sites of Cuprite mining district in Nevada [1].

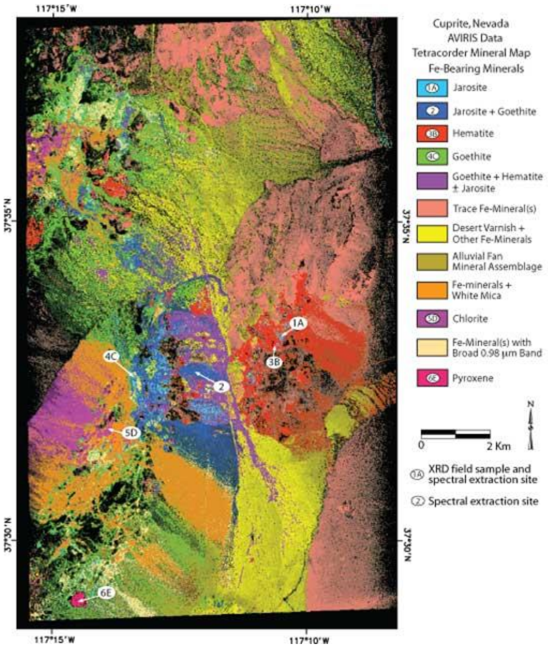

Figure 3-2: SI can determine the geological map of different mineral in Cuprite mining district in Nevada [1].

3.1.2 Food industry

SI is used in food industry as a non-destructive technique for product quality and safety control [41, 45]. Some examples are surface defects detection in apples, oranges and citrus [2, 46, 47], estimation of the firmness of strawberries [48], meat quality evaluation [49], detection of harmful contamination such as feces or agrochemical residues on foods [45, 50]. All these applications use the dissimilarity between the spectral response of different materials and the ability of SI to distinguish these dissimilarities. Figure 3-3 shows the spectral images of a number of Golden Delicious apples [2]; some are normal apples and some with surface defects. The shown images are three slices of spectral data cube at 542, 682 and 752 nm. It can be seen that the surface defects and the normal skin of apples can be distinguished in these spectral images.

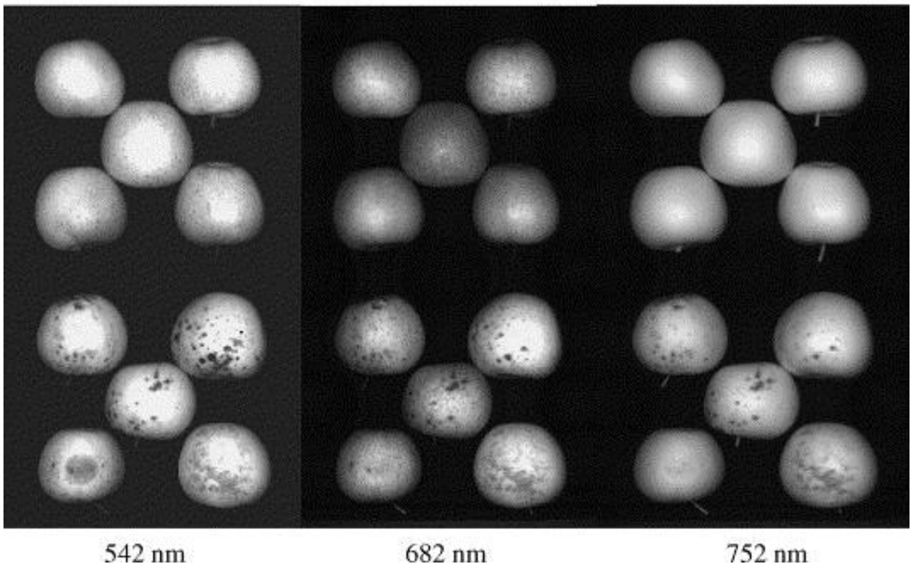

Figure 3-3: Spectral images of Golden Delicious apples at three 542, 682 and 752 nm. [2]

3.1.3 Medical applications

SI has found many applications in medical fields [42]. Two areas where the medical applications of SI have been heavily studied are disease diagnosis and surgical guidance. The optical and spectral properties of the tissue change upon the development of the disease and SI can detect this change for each pixel of the data cube. Figure 3-4 shows how SI detects the difference between spectral characteristics of muscle tissue and tumor tissue on a slice of sample tissue from a tumor-bearing mouse [3]. Studies have shown the capability of SI for cancer diagnosis in cervix [51, 52], skin [53, 54], ovary [55], colon [56, 57], oral tissue [58, 59], etc. SI also has the potential to provide guidance during surgical procedures. This potential has been widely explored in literature [42]. The difference between spectral properties of normal and cancerous tissue makes SI capable of helping the surgeon to maximize the removal of cancerous tissue while avoiding removal of healthy tissue. The

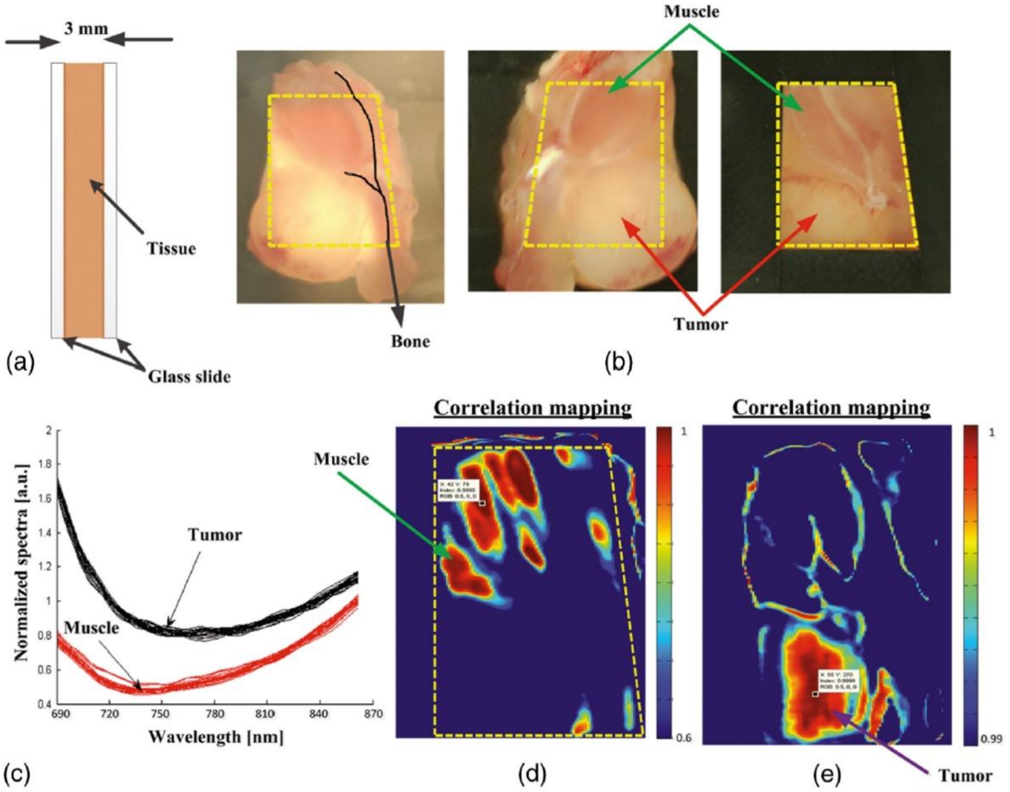

(a) Cross-section diagram of tissue sample for angular-domain spectroscopic imaging testing. (b) Color photographs of mouse tumor tissue sandwiched between two glass slides. The opening due to the black mask that was used for transmission imaging is marked by the yellow dashed line. The black line (left panel) indicates the location of bone embedded in the tissue. (c) Normalized spectra from regions of tumor and muscle tissue [as indicated in (b)]. (d) Correlation map of data cube based on reference spectral signature related to the muscle tissue. (e) Correlation map of data cube based on reference spectral signature related to the tumor tissue.

Figure 3-4: SI detects the difference between spectral characteristics of muscle tissue and tumor tissue on a slice of sample tissue from a tumor-bearing mouse [3].

spectral imager should operate in real-time fashion during the surgery for these type of applications. Many researches have investigated the intraoperative capabilities of SI in various surgeries such as cholecystectomy [60], nephrectomy [61] and abdominal surgery [62].

3.2 Spectral imaging methods

Conventionally there are two categories of approaches for SI: wavelength-scanning and spatial-scanning approaches [63]. Wavelength-scanning approaches capture the entire spatial data at once on a two-dimensional imaging sensor and then use a mechanism to scan in spectral domain. In contrast, spatial-scanning approaches capture the entire spectrum of a line of the object at a time and then spatially scan through the object in two-dimensional spatial domain to form the complete data cube.

Wavelength-scanning category of approaches apply spectral filters to either the source or the light impinging on the detector in order to scan in wavelength domain and cover the spectral range. This can be done by placing a rotating filter wheel [64] or a tunable filter [65] in front of either the light source or the sensor of a monochromatic camera. The wavelength scanning methods, in general, offer high spatial resolution that is the same as the spatial resolution of the monochromatic camera; however, the achievable spectral resolution is limited to the number of filters on the wheel or the spectral resolution of the tunable filter.

The filter wheel has a number of narrowband optical filters mounted on its perimeter and as the wheel rotates, one of the filters is in front of the sensor or the light source at a time. In this way, spectral images are captured at the passband wavelength of the filters in a sequential manner. Some of the disadvantages associated with using a filter wheel are low spectral resolution, narrow spectral range, mechanical vibration due to rotation of the wheel and slow speed of wavelength switching [66]. Another possibility is the application of a tunable filter in place of a filter wheel. Two common types of electronically tunable filters used in SI are acousto-optic tunable filters and liquid crystal tunable filters. Since the passband wavelength of these tunable filters is controlled electronically, they do not suffer from the mentioned disadvantages associated with filter wheels such as mechanical vibration. Furthermore, they offer rapid tuning speed over a broad spectral range [42, 65].

In spatial-scanning category of SI methods, a wavelength-selective element such as a grating or a prism gives the spectrum of one line of the object at a time. Scanning across the object is required to find the spectrum of whole object. This category of methods, in general, offers high spectral resolution that is the same as the spectral resolution of the wavelength-selective element; however, the required spatial scan limits the achievable spatial resolution.

The wavelength-selective element is a key part of spatial-scanning spectral imagers. The most commonly used wavelength-selective elements are gratings [67, 68] and prisms [54, 69]. Another dispersive element used for SI applications is prism-grating-prism [70, 71]. prism-grating-prism consists of a specially designed transmission grating sandwiched between two symmetrical or nearly symmetrical prisms [72]. Some advantages of spectral imagers with prism-grating-prism are small size, ease of mounting and straight optical axis [72].

Interferometric SI [73, 74] is another technique that combines a Fourier transform spectrometer and a focal plane array. The spectral imager collects a sequence of images of the scene through an interferometer by changing the interferometric optical path difference. The change in interferometric optical path difference translates the spectral information into a temporal interferogram. The Fourier transform of the interferogram for each pixel is required to transform the information to frequency domain and produce the spectral data cube.

Both wavelength-scanning and spatial-scanning methods capture only two dimensions of the data cube at a time and scan in the third dimension. Recently some snapshot SI techniques have been introduced that capture all three dimensions in a snapshot without scanning. Splitting the aperture is one approach to snapshot SI. Mathews [75] reported a SI system consisting of a single charge-coupled device (CCD) and an array of 18 individual lenses coupled to individual spectral filters. The combination of 18 sub-images create a composite image. Sampling the field of view is another approach for snapshot SI. Matsuoka et al. [76] divided the field of view into 10 by 10 sections which is sampled by a bundle of 100 fibers. A grism (a composite device of a grating and a prism) creates the dispersed spectrum of each fiber. Similarly, SI system introduced in [77] uses a lenslet array and/or a pinhole array to reimage and divide the field of view into multiple channels. A prism disperses the multiple channels into multiple spectral signatures. Although these techniques collect the entire data cube simultaneously, they compromise the optical throughput and/or spatial resolution to achieve that.

The computed tomography imaging spectrometer [78-81] is another non-scanning instrument capable of simultaneously acquiring full spectral information from every position within its field of view. The spectral imager includes a computer-generated-hologram which maps the scene on a detector array as a function of both position and wavelength. A change in the wavelength results in the expansion or contraction of the diffraction pattern within the focal plane. A change in position results in a corresponding translation of the diffraction pattern across the focal plane. Therefore, the detector array contains all the required information to construct the data cube. Mathematical algorithms are used to invert this mapping and construct the data cube. In other words, computer-generated-hologram maps the three-dimensional object space, (x,y,λ), to a two-dimensional detector array [78].

Coded aperture [82-84] is another single-shot SI approach. This technique uses a binary coded aperture and the concept of compressive sensing to form the spectral data cube from smaller number of compressed measurements relative to the size of the final reconstructed data cube. The imager consists of a coded aperture, a dispersive element and a detector. The coding is applied to the source field by a coded aperture. The resulting coded field is subsequently modified by a dispersive element before it impinges onto the detector. Reconstruction algorithms will calculate the spectral data cube from the compressive measurements across the detector [84].

Another single-shot spectral imaging technique is called image mapping spectroscopy [69, 85]. A relay lens first creates an image of the object on an array of densely packed tiny mirror facets. These mirrors then redirect portions of the image to different regions of a collecting lens pupil. A dispersing prism located in the pupil disperses these portions of the image. A re-imaging lens array then re-images the dispersed portions of the original image onto the image sensor. With this technique, there is no compromise of optical throughput or spatial resolution as the mirror facets are smaller than the incident point spread function and highly reflective [69, 85].

The most important factors for SI techniques are spatial resolution, spectral resolution, optical throughput, acquisition time and cost. Most SI techniques have some sort of tradeoff between these factors. In spatial-scanning techniques, for instance, there is the tradeoff between acquisition time and spatial resolution. This is because the spectrum of a line of the object is calculated at a time. Thus, in order to improve the spatial resolution, the line scanning must be done in finer steps which results in longer acquisition time. In addition, since these techniques include a dispersive element such as a grating or prism, they also have the inherent tradeoff between optical throughput and spectral resolution that exist in these dispersive elements. The tradeoff comes from the fact that a narrower exit slit provides better spectral resolution but smaller optical throughput. Wavelength-scanning techniques, on the other hand, are limited by the tradeoff between spectral resolution and acquisition time for similar reasons.

Depending on the application, some of the four mentioned factors are of greater importance. For example, in real-time inspection of food products at industrial production lines, the time required to form the data cube and the cost are crucial but a very high spectral resolution might not be necessary. In many medical and remote sensing applications, on the other hand, high spectral and/or spatial resolutions are necessary but higher cost and lower speeds might be tolerated.

In Chapter 4 of this dissertation, we introduce a novel spectral imaging technique. Using this technique, both spectral and spatial resolutions can be improved simultaneously and independently. The spectral imager is also low-cost and compact. The technique will be explained in details in Chapter 4.

3.3 Summary

SI is measuring the intensity of a scene as a function of position and wavelength. A review of SI techniques and their applications was given in this chapter. SI has found applications in various fields. Examples of SI applications in remote sensing, food industry and medical imaging were briefly discussed. A review on existing SI techniques in the literature was also given in this chapter. The most important factors for assessing SI techniques are spatial resolution, spectral resolution, optical throughput, acquisition time and cost.

CHAPTER 4 : SPECTRAL IMAGING BASED ON CHROMATIC ABERRATION

This chapter introduces a novel spectral imaging (SI) technique. The introduced spectral imager consists of a dispersive lens system and a computational unit. The main idea is to make use of chromatic aberration of a lens system to disperse and separate the spectral information of the object (see Figure 4-1). A highly dispersive imaging lens system is designed for this purpose. Due to dispersion, the lens system has a focal volume instead of a focal plane. As a result, the location of the focused image of a flat multicolor object formed by the dispersive lens system is wavelength dependent; in other words, each wavelength has its own conjugate image location. Therefore, the location of focused image can be related to spectral content of the object. The role of the computational unit is to find the location(s) of the focused image(s) for any point across the field of view and to calculate the spectral information of the object based on these location(s).

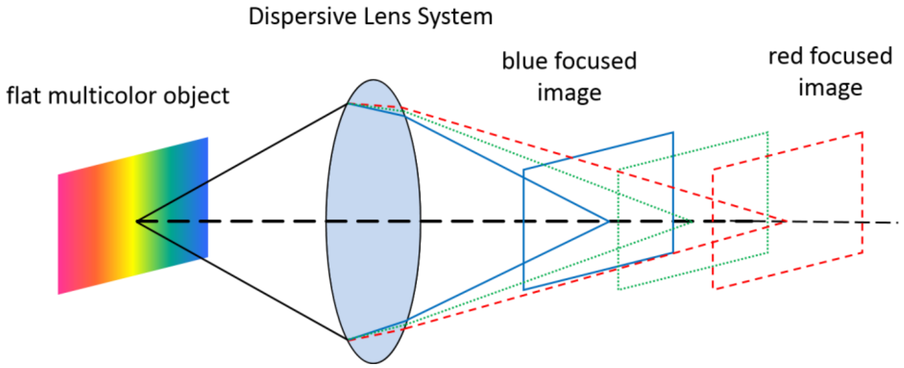

Figure 4-1: Layout of the novel spectral imaging technique

The spectral resolution of the introduced spectral imaging technique is affected by the amount of chromatic aberration produced by the lens system and by the ability of the computational unit to locate the focused images. The spatial resolution, on the other hand, is determined by the spatial resolution of the lens system. Therefore, these two resolutions can be improved simultaneously. As discussed in Chapter 3, some of the most important parameters for assessing and selecting a SI technique for the desired application are spatial resolution, spectral resolution, optical throughput, acquisition time and cost. It was also mentioned in Chapter 3 that conventional SI techniques introduce some kind of tradeoff between these parameters. Using our SI technique one can, in principle, improve both spectral and spatial resolutions simultaneously. Our spectral imager is also low cost and compact. The time required to calculate the data cube is limited by the computational unit and mechanical movement of the imaging sensor. These parameters will be investigated in more details in this chapter.

4.1 Dispersive lens system design

A main component of our spectral imager is a dispersive imaging lens system. The ideal lens system for our purpose ought to fulfill two criteria: it should be highly dispersive and yet it should still form good-quality images. When designing an imaging system, designers usually try to avoid all types of aberrations including chromatic aberration. Here, we are taking advantage of the chromatic aberration to separate and disperse the spectral information of the object over its focal volume. Therefore, the chromatic aberration is desired and aimed to be maximized during the design. In fact, the larger is the chromatic aberration, the better spectral resolution can be achieved by the spectral imager. However, except for chromatic aberration, other aberrations are undesirable and aimed to be minimized in order to maintain the quality of the images and the spatial resolution of the camera. In summary, we would like to design a lens system that has a distinctive image location for each wavelength but forms a perfectly in-focus image for all wavelengths on their corresponding image locations.

Considering these criteria, an imaging lens system was designed. For reasons explained in the following paragraph, we designed a three-element Cooke triplet for our spectral imager. For the sake of simplicity and cost, we limited ourselves to three spherical elements in this design. However, the performance of the spectral imager can be improved both spectrally and spatially by adding more elements to the lens design and by using aspheric surfaces.

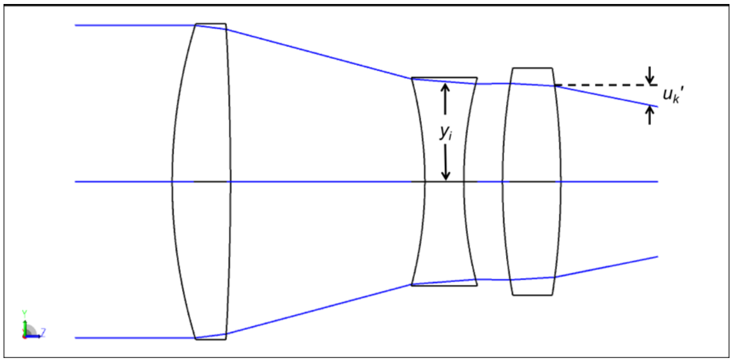

Figure 4-2: The Cooke triplet

Cooke triplet (see Figure 4-2) consists of a negative singlet element surrounded by two positive singlet elements. There are eight degrees of freedom in the design: six surface curvatures and two airspaces between the elements. An interesting point about Cooke triplet is that there are enough available degrees of freedom to control all seven primary aberrations (five third-order Seidel aberrations plus axial and lateral color). Another important degree of freedom in designing a Cooke triplet, besides the curvatures and airspaces, is the choice of material for the lens elements. Material selection is an important factor that significantly affects the final performance of the lens system. Next section discusses, in details, the significance of material selection in our design and the approach that we took to do this in a way that helps us achieve our design criteria.

4.1.1 Material selection

The choice of materials is an additional degree of freedom in Cooke triplet design. Although material selection does not add a continuous variable and there are only discrete choices available but it can significantly change the final performance of the triplet. In order to correct the axial chromatic aberration, normally a crown type material (lower dispersion or higher Abbe number) is selected for the positive lenses and a flint type material (higher dispersion and lower Abbe number) is selected for the negative lens. Two positive lenses are usually made of the same material since this helps with keeping the design symmetrical and there is no benefit in using different materials. Axial chromatic aberration of an assembly of thin lenses can be calculated from equation (4-1) [86]:

$$TA_{ch}A = \frac{1}{u_k{}'}\Sigma\frac{y_i^2\Phi_i}{V_i} \tag{4-1}$$

where $TA_{ch}A$ is the axial chromatic aberration, $u_k{}'$ is the marginal ray angle after refraction from the last element (or at image), y_i is the marginal ray height at each element, Φ_i is each element's power and V_i is the Abbe number of the material of each element (see Figure 4-2). Since the sum of powers and the marginal ray height are higher for positive elements compared to the negative element, the Abbe number of the material of the positive lenses should be higher too in order to reduce the chromatic aberration to zero. Therefore, minimizing the axial chromatic aberration is one of the reasons for why choosing crown and flint type materials for positive and negative lenses, respectively, is the proper choice.

Apart from the Abbe number, the refractive indices of the crown and flint type materials plays an important role in the design as well. Choosing a crown type material with a high refractive index leads to larger surface curvatures and helps in minimizing higher order aberrations and improving the performance of the triplet. Moreover, the positive elements made of a higher index material and the negative element made of somewhat smaller index material would help to reduce Petzval sum. The Petzval sum for a number of thin elements is calculated by the following equation [86]:

$$TPC = \frac{h^2}{2{u_k}'}\Sigma\frac{\Phi_i}{n_i} \tag{4-2}$$

where TPC is the transverse third-order Petzval sum, h is the image height, n_i is the refractive index of the material of each thin lens element and ${u_k}'$ and Φ_i are as defined in equation (4-1) and shown in Figure 4-2. Therefore, minimizing the Petzval sum is another reason for choosing crown and flint type materials for positive and negative lenses, respectively.

Another thing to consider while selecting the material types is that the difference between the Abbe numbers of the crown and flint materials affect the total length of the design. A small difference between the Abbe numbers would drive the airspaces to smaller values and the lenses would be closer to each other in final design. In contrast, a large difference between the Abbe numbers would result in more separated lenses and a more stretched out final design.

It should be reminded that here we are interested in lens designs with high axial color and we do not have any intention to zero the value of the sum in equation (4-1). On the contrary, we would like to increase the chromatic aberration as much as possible. Therefore, we need to adopt a different approach in material selection from the normal approach for designing a Cooke triplet. In contrast to normal material selection approach, we need a material with smaller Abbe number for positive lenses and high Abbe number for the negative lens to increase the axial color calculated from equation (4-1). However, large values of refractive indices and a somewhat larger refractive index for positive lenses compared to the negative lens are still desirable to reduce Petzval sum and higher order aberrations. To summarize, a material from the lower left part of glass map for the negative lens and a material from the upper right part of the glass map for positive lenses are suitable for our purpose. We also tried to use low-cost and commonly used materials for this design.

With these points in mind, Schott N-SF10 (n_d of 1.7283, V_d of 28.5) is chosen for the positive elements and Schott N-Bk7 (n_d of 1.5168, V_d of 64.2) is chosen for the negative element. n_d is the refractive index at the wavelength of d spectral line which is 587.6 nm and V_d is the Abbe number at this wavelength and is calculated from equation (4-3):

$$V_d = \frac{n_d - 1}{n_F - n_C} \tag{4-3}$$

where n_F and n_C are the refractive indices of the material at F and C spectral lines which are 486.1 nm and 656.3 nm, respectively.

4.1.2 The designed lens system

Figure 4-3 illustrates the layout of the designed lens system along with information about the curvature, thickness, material and aperture of each surface. In our lens design,

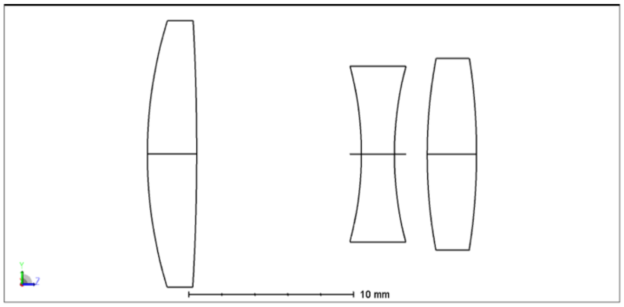

radius [mm]	thickness [mm]	material	semi-aperture [mm]
27.66	3.00	N-SF10	8.08
-140.55	10.01	air	8.08
-20.69	2.00	N-BK7	5.33
20.69	2	air	5.33
32.33	3.00	N-SF10	5.82
-38.71		air	5.82

Figure 4-3: The designed dispersive lens system

the target effective focal length (EFL) is 40 mm and the f-number is 2.5. We use a Point Grey Flea3 [87] monochromatic charge-coupled device (CCD) as our image sensor. The sensor size is 6.78 mm by 5.43 mm. The lens system is optimized for finite/finite object and image conjugate distances. The field of view of the spectral imager depends on the object distance or in other words the magnification of the system. Smaller magnification means larger FOV but it also means larger object distance and hence smaller object-space numerical aperture (NA). Larger NA becomes more important in low light conditions where we need the lens system to gather more light from the object. Therefore, the object distance can be chosen based on the FOV and object-space NA. We use the same lens system in two different configurations; one configuration has magnification of -1 ($M = -1$) and the other has magnification of -0.5 ($M = -0.5$). The spot size and as a result the spatial resolution of the designed lens system differs slightly depending on the chosen FOV.

During the design process, some constraints are applied to the thicknesses of the lenses and the airspaces. The airspaces between the lenses are forced to be larger than 2mm, the center thickness of the positive lenses and negative lens are forced to be larger than 3 mm and 2 mm, respectively. The lens system was optimized for visible range, more specifically for F (486.13 nm), d (587.56 nm) and C (656.27 nm) wavelengths. The system is designed to have EFL of 40 mm at d wavelength. The system's EFL is 38.44 mm at F and 40.66 mm at C wavelength. Therefore, the chromatic aberration produced by the lens system separates F and C focal lengths by 2.22 mm. This separation between F and C focal lengths would translate into 8.82 mm separation between F and C image planes when the magnification is -1 and 4.82 mm separation between F and C image planes when the magnification is -0.5. In next section, we discuss what these numbers mean in terms of the spectral resolution of our spectral imager.

4.1.3 Spectral and spatial resolution of the spectral imager

Let us assume that the object is a point source with two spectral lines or with spectral content at two wavelengths only. We want to resolve these two wavelengths with our spectral imager. The lens system would form a focused image of the point source at two locations, one location for each spectral line. In order to resolve these two wavelengths, the spectral imager has to distinguish and resolve these two focused image locations. However, even for a diffraction limited lens system a point would be imaged to not a point but an intensity distribution, i.e. the point spread function (PSF), both perpendicular to the optical axis (transverse PSF) and along the optical axis (axial PSF). The transverse intensity distribution of the PSF of a diffraction-limited lens is the well-known Airy disk distribution. However, what affects the spectral resolution of our imager is the axial intensity distribution along the optical axis because that is what determines the ability of the lens system to distinguish two axial focus locations. The distribution of intensity along the optical axis in and around the paraxial image plane due to diffraction is expressed as [88]:

$$I = I_0 \left[\frac{\sin(\pi \tilde{z})}{(\pi \tilde{z})} \right]^2, \qquad \tilde{z} = \frac{\mathrm{NA}^2 z}{2n' M^2 \lambda} \tag{4-4}$$

where I_0 is the peak intensity at paraxial image location, z is the axial distance from the paraxial image location along the optical axis, NA is the numerical aperture, n' is the refractive index of the image space, M is the transverse magnification of the lens system and λ is the wavelength. The diffraction depth of focus can be defined as the axial distance for which the axial PSF becomes zero:

$$\text{diffraction depth of focus} = 2n' \frac{M^2 \lambda}{\mathrm{NA}^2} \tag{4-5}$$

If we assume the closest two axial PSFs can get and still be resolved is when the first zeros of one PSF coincides with the maximum of the other PSF, then the axial distance between the two PSFs should be larger than diffraction depth of focus in order for them to be resolved by the lens system. This means in order for our spectral imager to resolve two spectral lines in the object, the distance between the images of these two spectral lines has to be larger than diffraction depth of focus. This is all for the case of diffraction-limited optical performance.

Please note that the diffraction depth of focus in equation (4-5) is a function of wavelength, λ. In addition to that, the magnification of our dispersive lens system also changes with wavelength. Therefore, the resolution of the spectral imager is a function of wavelength and is not uniform over the spectral range. For a refractive lens system, smaller wavelengths are focused closer to the lens system. Hence, both λ and M in equation (4-5) increase with wavelength and the resolution deteriorates for larger wavelengths.

The next step would be to transform a minimum axial distance between the two images (Δz) into a minimum wavelength difference between the object's two spectral lines ($\Delta\lambda$). In reality, as shown in Figure 4-3, the location of focused image is not a linear function of wavelength. Furthermore, as discussed in previous paragraph, the minimum axial location itself is a function of wavelength and is not constant over the spectrum. This means Δ_{z1} and Δ_{z2} are not equal in Figure 4-3. However, if we assume the dispersion of the system is linear and the diffraction depth of focus is independent of wavelength, which none of them are true, then the axial separation of Δz is related to wavelength separation of $\Delta\lambda$ by the following equation:

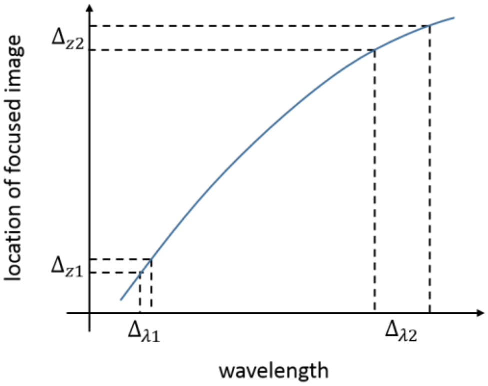

Figure 4-4: The location of focused image is not a linear function of wavelength and thus, there is not a linear relation between Δz and $\Delta\lambda$. Furthermore, Δz itself is a function of wavelength and is not constant over the spectrum.

$$\Delta\lambda = \frac{\lambda_C - \lambda_F}{z_C - z_F}\Delta z \tag{4-6}$$

where λ_C is 656.27 nm, λ_F is 486.13 nm, z_C is the axial image location of C wavelength and z_F the axial image location of F wavelength. As discussed above, the nonlinearity of the dispersion of the lens system and the dependency of the diffraction depth of focus on wavelength would result in non-uniform spectral resolution of the spectral imaging system for different spectral ranges. Despite this, equation (4-6) is a good approximation to convert axial resolution to spectral resolution. In order to calculate the diffraction-limited spectral resolution, we calculate Δz from equation (4-5) at $\lambda = 587.56\,nm$ (d wavelength) and substitute that into equation (4-6). In this way, we can calculate the spectral resolution at d wavelength and that is the number that we report as the diffraction-limited spectral resolution of our spectral imager.

Figure 4-5 shows the designed lens system for both $M = -1$ and $M = -0.5$ configurations. The specifications of each configuration are summarized in a table, also shown in the figure. Using equation (4-6) to convert diffraction depth of focus to spectral resolution, we obtain that the diffraction-limited spectral resolution is about 2.0 nm for both $M = -1$ and $M = -0.5$ configurations, respectively. Although the separation between F and C image locations is larger for $M = -1$, the diffraction depth of focus is also larger proportionally. Therefore, equation (4-6) results in similar spectral resolutions for both configurations.

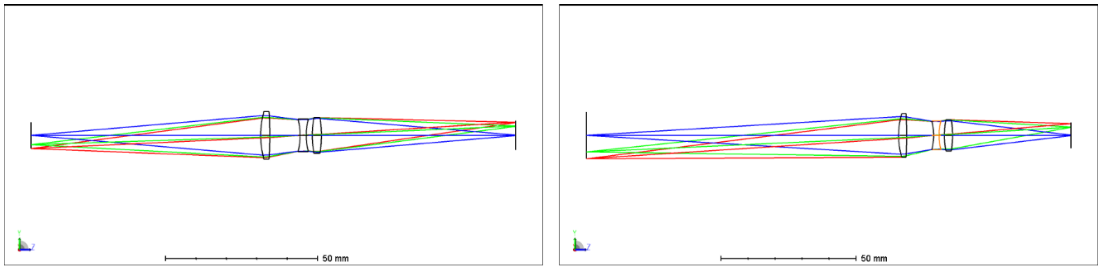

(a) (b)

	(a)	(b)
magnification @ d wave	M = -1	M = -0.5
field of view	6.78 mm x 5.43 mm	13.56 mm x 10.86 mm
object-space NA	0.106	0.070
z_F - z_C	8.82 mm	4.82 mm
max RMS spot size across the field	39 μm	46 μm
diffraction depth of focus	105 μm	60 μm
diffraction-limited spectral resolution	2 nm	2.1 nm

Figure 4-5: The designed lens system in two configurations (a) $M = -1$ and (b) $M = -0.5$. The specifications of each configuration is summarized in a table also shown in the figure

Equation (4-6) calculates the theoretical limit in spectral resolution of our SI technique that comes from the diffraction depth of focus. However, our lens system performance is not close to the diffraction limit and its resolution is worse than the theoretical limit. The actual working resolution of our designed spectral imager is calculated in section 4.1.3. There, two spectral lines are introduced in the object's spectrum. Then, the wavelengths of these two spectral lines are brought closer together until the spectral imager does not resolve them anymore. The closest that these two wavelengths can be while our spectral imager can still differentiate between them is reported as the actual resolution of the designed spectral imager. The process is repeated after adding different levels of noise to the system.

Spatial resolution of our spectral imager is the same as spatial resolution of the designed lens system. For our Cooke triplet lens system, it is the lens spot size rather than the CCD pixel size that restricts the spatial resolution. The maximum root mean square (RMS) spot size of the lens system over the field of view is reported in Figure 4-5 for both magnifications. The maximum RMS spot size is 39 microns for $M = -1$ and it is 46 microns for $M = -0.5$ configurations. This would give us the spatial resolution of the spectral imager in each configuration.

Now that the dispersive imaging system is designed, we need an algorithm to analyze images formed by the lens system and calculate the spectral information of the object. Next section is devoted to explaining the role of the computational unit and the algorithm that the unit uses to locate the focused image.

4.2 Computational unit

Due to its dispersive characteristics, the designed lens system has a focal volume instead of a focal plane. As a result, the imaging system does not image a point of the object to a unique image location; each wavelength in the spectrum of the point has its own conjugate image location. Assuming that the object is flat and without any depth variation, any location in the image space of the lens system can be associated to a wavelength through a calibration process. Although the entire spectral information of the object would exist on every image captured at any location, only the spectral information corresponding to one wavelength would form a sharp and focused image on that plane. This specific wavelength is the wavelength associated to that location. For instance, the image location corresponding to F wavelength is 57.8 mm away from the last lens for the designed system. If the camera acquires an image at this location, although all the existing colors in the object contribute to the formed image but it is only the F wavelength that is sharp and focused at this location. All the other colors form blurred and defocused images. We need to distinguish between the focused and defocused images at every location in order to find the spectral information of the object. It is, therefore, possible to correlate the sharpness of the image with spectral information of the object and the problem of calculating the spectral information of the object comes down to finding the location(s) of focused image for every pixel of the object. Each focused image corresponds to a spectral content of that pixel.

Finding the location of focused image is also of interest in 3D imaging where 3D depth map of an object is reconstructed from captured 2D images. In this section, we start with explaining how the problem of finding the focused image location is addressed in 3D imaging and then we will explain how the algorithms used for 3D imaging can be also applied to our spectral imager.

4.2.1 Shape from focus

An overview of some of the 3D surface reconstruction techniques was given in Chapter 2. Among these techniques, shape from focus is the one that is implemented in the computational unit of our spectral imaging camera. Shape from focus, as discussed in section 2.2.1 and depicted in Figure 2-3, is a well-known passive algorithm widely used for 3D surface reconstruction. For convenience, Figure 2-3 is shown again in Figure 4-6.

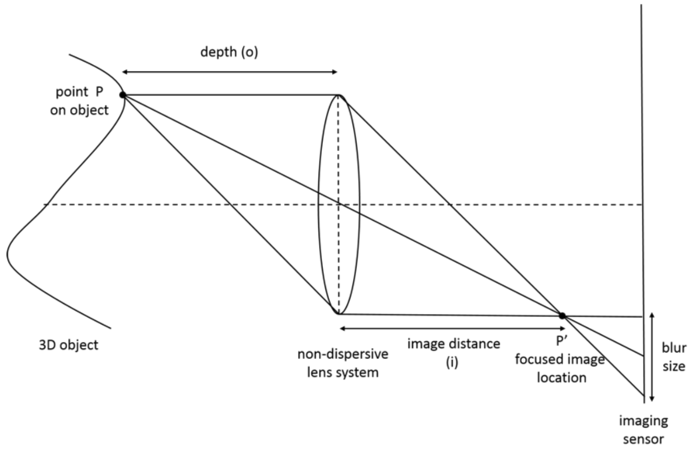

Figure 4-6: A focused image of the point P on the 3D object is formed by the lens system at P'. The location of P' depends on the depth of point P. Shape from focus algorithm searches for the location of P' and uses that to calculate the unknown depth of the point P.

The imaging system used for 3D imaging is ideally non-chromatic but the object is 3D. The image of each point on the object is blurred based on its depth or in other words its distance from the imaging system. Basic idea behind shape from focus algorithm is that if the location of focused image (P' in Figure 4-6) is found for point P on the object, with the camera parameters assumed to be known, the distance of point P from the camera can be calculated from the lens equation:

$$\frac{1}{f} = \frac{1}{o} + \frac{1}{i} \tag{4-7}$$

where f is the focal length, o is the object distance (depth of point P) and i is the image distance (location of P'). Shape from focus algorithm needs a sequence of images acquired at different distances from the lens system. Once this stack of images is captured, the algorithm searches for the sharpest image in the stack. When the image location (i) is determined, equation (4-7) can be used to calculate the object distance or depth (o).

4.2.2 Spectrum from focus (SFF)

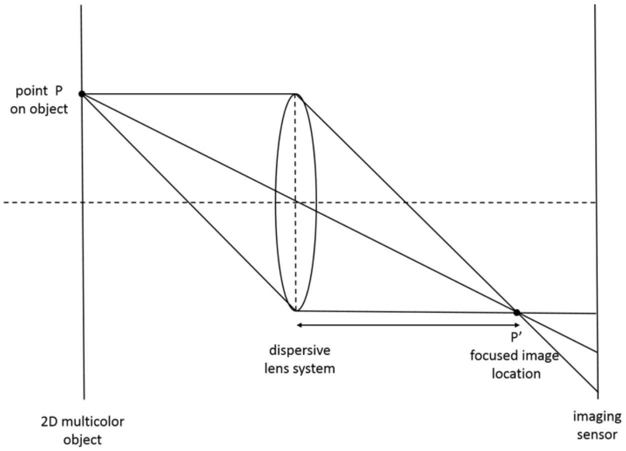

Figure 4-7: A focused image of point P on the object is formed by the lens system at P'. The focal length of the lens system and hence the location of P' depends on the spectral content of point P. Spectrum from focus algorithm searches for the location P' and uses that to calculate the unknown spectrum of P.

In our spectral imager, we are solving a similar problem to 3D imaging. The designed dispersive lens system in section 4.1 spreads the spectral information of the object over a volume. The computational unit uses the images produced by the dispersive lens system to compute the spectral images of the object. As mentioned earlier, the computational unit does so by searching for location(s) of focused image for every point of the object. Once those locations are determined, the spectrum of the object can be computed consequently. Therefore, we have a similar scenario to 3D imaging. The difference is that instead of the depth map of a 3D object, the spectrum of a flat object is of interest and the imaging is done by a highly dispersive lens system (see Figure 4-7). In our case, it is the spectral information of each point, not its depth, that changes the focal length of the lens system and makes the image blurred. However, the concept is the same. Shape from focus algorithm can be applied to images captured by the designed dispersive lens system and spectral images of the object can be calculated. Throughout this dissertation, the algorithm used by the computational unit of our spectral imager is referred to as spectrum from focus (SFF) because it is used for spectrum calculation not depth calculation. In the rest of this section, we will explain how this algorithm is applied to images formed by the dispersive lens system to calculate the spectrum of the object.

If a flat but multicolor object is placed in front of the designed dispersive lens system, each color of the object forms a focused image at a specific location. This is because the focal length of the lens system is a strong function of wavelength. The lens system and its dispersive characteristics are fully calibrated and known to us. Therefore, each location of focused image can be related to a wavelength. A sequence of images is captured at different distances from the lens system. SFF searches for the focused image(s) and then uses the location of focused image(s) along with the known camera parameters to calculate the spectral information. The main challenge here is measuring the sharpness of each captured image and locating the focused image. Using SFF algorithm for calculating spectral images requires an axial scan to move the detector but once the stack of images is captured, the spectral information of whole field of view is calculated simultaneously.

In this chapter, we assume that the object is flat and does not have any depth variation so that the location of focused image is a function of the spectral content of the object only and not its depth. All the simulation and experimental results given in this chapter are flat but multicolor objects. In cases where the spectral images of a 3D object are of interest, we need to form a 2D image of the object first and use that as the input to our spectral imager. This can be implemented by using a fiber optic face plate [89]. A faceplate is a dense two-dimensional array of fibers that transfers an image pixel by pixel (fiber by fiber) from on face of the plate to the other. Therefore, if an image of the 3D scene is formed on one face of the faceplate, the other face can be used as the input to our spectral imager.

The computational unit requires measuring the level of sharpness or focus for each pixel of the image at each captured image. Various criteria or operators for assessing the degree of focus at a pixel are proposed in the literature [17]. The gradient or first derivative of intensity is an intuitive focus measure operator to determine how much in focus is a pixel. The gradient of intensity is expected to be higher for a focused image compared to a blurred one due to presence of sharp edges. The high frequency content of an image is another indicator of presence of sharp edges and hence the degree of focus. The gradient-based operators are sensitive to the size of the local evaluation window over which the gradient is calculated. The focus measure operators that look at the high frequency content, on the other hand, are less sensitive to evaluation window size but more sensitive to noise because noise also contributes to the high frequency content of the image.

The coefficients of the discrete wavelet transform contain information about frequency and spatial content of an image and hence can be used as a tool to measure the high frequency content and focus level of an image. Here we use the ratio between the high frequency coefficients, M_H, and the low frequency coefficients, M_L, of the discrete wavelet transform as a focus measure [90]. In the first level discrete wavelet transform, the image is decomposed into four sub-images: W_{LH1}, W_{HL1}, W_{HH1} and W_{LL1}. First three are detail sub-bands and the last one is the coarse approximation sub-band. For a higher-level discrete wavelet transform, the coarse approximation itself is decomposed into detail and coarse sub-bands. Equations (4-8) to (4-10) from reference [17] are applied to each pixel of each captured image to determine the level of focus at that pixel:

$$\text{focus measure} = \frac{M_H^2}{M_L^2} \tag{4-8}$$

$$M_H^2 = \sum_{k} \sum_{(i,j)\in\Omega} W_{LHK}(i,j)^2 + W_{HLK}(i,j)^2 + W_{HHK}(i,j)^2 \tag{4-9}$$

$$M_L^2 = \sum_{k} \sum_{(i,j)\in\Omega} W_{LLK}(i,j)^2 \tag{4-10}$$

where Ω is the local window and sub-index k indicates the level of wavelet transform. The first level coefficients are used in equation (4-9) ($k = 1$) and the third level coefficients are used in equation (4-10) ($k = 3$). The local window size is fixed to 7x7 pixels in our computations.

Something that must be noted is that the magnification of the lens system is not the same for all images in the captured image stack. As the CCD moves along the optical axis, the magnification of the lens system varies accordingly. Therefore, each image of the image stack is imaging a slightly different area of the object from its adjacent image in the stack. The image that has the largest distance from the lens system, has the largest magnification and images the smallest area of the object. The problem that this change of magnification causes for the SFF algorithm is that the same pixel in two images do not represent the same position in the object space. This issue can be addressed either in hardware by designing a telecentric lens system or in software [91]; we use the latter. The image captured at the farthest position from the lens system is taken as the reference. All images in the image stack are scaled accordingly with respect to the reference image to show the same area as if they have the same magnification. Matlab’s intensity-based image registration function, *imregister*, is used to scale all images. They are all registered with regard to the reference image. Once this correction is done, it is assumed that a specific pixel on all the images in the image stack corresponds to the same point of the object.

Another point worth mentioning is that one drawback of passive 3D depth measurement techniques in general is that they work only for the scenes or objects that have some natural texture on the surface. Shape from focus algorithm like other passive depth measurement techniques suffers from this limitation. The texture is required for the algorithm to be able to accurately measure the sharpness of each image. This is also true when SFF algorithm is used by our spectral imager to calculate the spectral images of an object. The algorithm needs textured targets.

When a focus measure value is assigned to each pixel of each image in the image stack, we look at the behavior of the focus measure for each pixel. Whenever the focus measure function peaks at a location, it means that the wavelength corresponding to that location exists in that pixel of the object. Next section shows some examples of how SFF algorithm is applied to images produced by the designed dispersive lens system.

4.3 Simulation results

In this section, results of applying SFF algorithm to some simulated images are discussed. Two sets of simulation are performed in Zemax. In the first set of simulations, the designed dispersive lens system shown in Figure 1 is simulated in Zemax non-sequential mode. Here rays from a point source with some spectral content are traced through the lens system to a detector which moves in axial direction and for each location the detector data is saved. Then the SFF algorithm is applied to these images to see how the focus measure function behaves as detector location is changed. The first set of simulation is not really spectral imaging since we are simulating a point source rather than an extended object. However, the results are useful in demonstrating the basic concept on which our spectral imager works. In addition, as we will see, this set of simulations are used to investigate the spectral resolution of our spectral imager. In the second set of simulations, Zemax sequential mode is used to capture images of an object formed by the designed dispersive lens system. The image location changes step by step and at each location an image is generated by Zemax '*Image Simulation*' tool. SFF is then applied to these images.

4.3.1 First set of simulations

In the first set of simulations, the designed dispersive lens system is simulated in non-sequential Zemax in M = -1 configuration. Figure 4-8 illustrates the layout of the simulation. A point source with three spectral lines at F, d and C spectral lines is used as the object. This would be equivalent to having three narrowband laser spots overlapping with each other at a point and used as the object for our spectral imager. Rays from this source are traced to a detector with the same size and pixel number as our Point Grey CCD. The detector moves in axial direction and the image is saved at each location. The detector is moved in 100 microns steps in distance range of 57 mm to 68 mm from the lens system. The simulated intensity distribution on the CCD for these 111 axial locations is saved. Some of these images are shown in Figure 4-9. It can be seen that the image goes through a series of focuses and defocuses as the detector moves in axial direction. The focus/defocus behavior is a function of spectral content of the source.

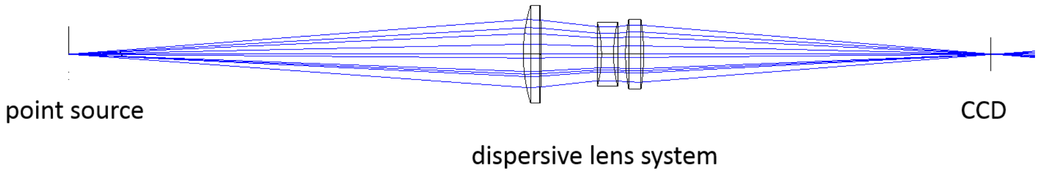

Figure 4-8: In the first set of simulations, the designed dispersive lens system is simulated in Zemax non-sequential mode

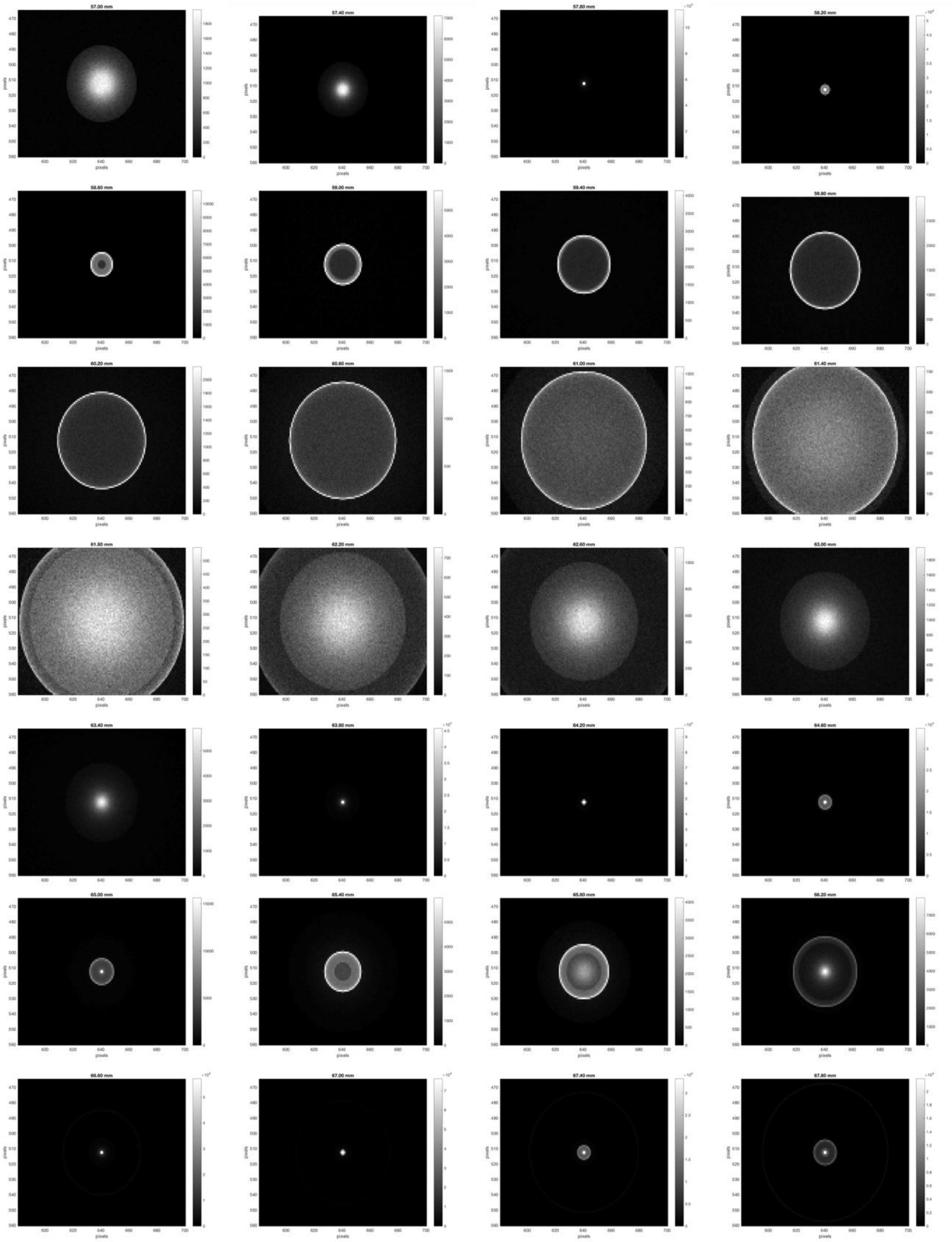

Figure 4-9: Intensity distribution simulated on the CCD at different distances from the lens system. These 28 images were taken in 400 micron steps in distance range of 57 mm to 67.8 mm from the lens system.

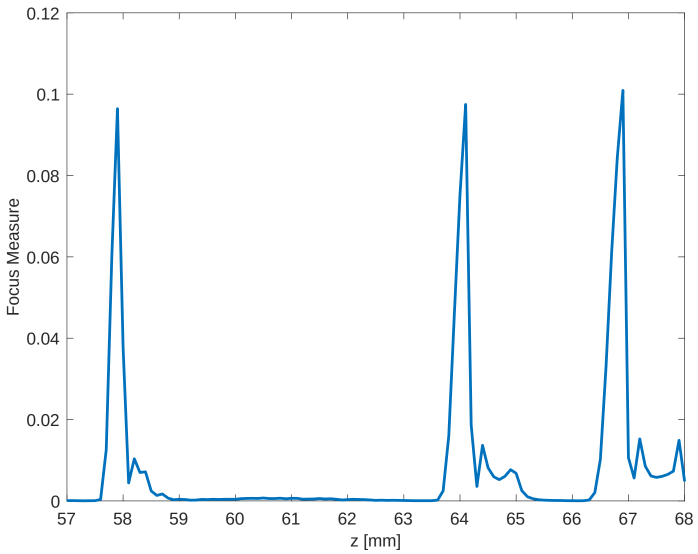

Figure 4-10: Focus measure function plotted versus axial distance from the lens system

If we apply SFF algorithm to the 111 captured images and plot the focus measure function introduced in equations (4-8)-(4-10) versus axial location, we would expect the function to peak at three locations that correspond to F, d and C image locations. The focus measure plot with the three expected peaks is shown in Figure 4-10.

Equation (4-6) calculates the limit in spectral resolution of our spectral imager that comes from the diffraction depth of focus. However, our lens system performance is not close to the diffraction limit. We used this set of simulations to determine the spectral resolution achieved by the designed lens system. In order to determine the resolution, we introduce two spectral lines in the object’s spectrum. The object in this case is a point source. One spectral line is F wavelength and the other one is F+$\Delta\lambda$. We start making $\Delta\lambda$ smaller and smaller and follow the focus measure function versus axial location until the two peaks in focus measure function cannot be resolved anymore. This would give the actual achievable spectral resolution of the spectral imager. Please note that as discussed in section 4.1.3, the resolution of the spectral imager is also wavelength dependent. Therefore, this set of simulations gives the spectral resolution only at F wavelength.

Figure 4-11 (a)-(d) illustrates the process of determining the spectral resolution. Figure 4-11 (a) shows the focus measure function as a function of distance from the lens system when the point source has two spectral lines, one at F wavelength and the other one at F+10 nm ($\Delta\lambda = 10$ nm). As expected, the focus measure function peaks at two locations each corresponding to one of the spectral lines in the source. The same process was repeated for $\Delta\lambda = 5$, 4, 3 and 2 nm. Figure 4-11 (b)-(d) shows the focus measure plots versus axial distance for these four $\Delta\lambda$ values. As $\Delta\lambda$ gets smaller, the two peaks in focus measure function become closer and finally they are not distinguishable anymore.

To find the limit where the peaks are not resolved by the lens system anymore and to determine the spectral resolution of the spectral imager, each spectral line was simulated separately. An object with a single spectral line is simulated and the simulation is repeated twice, once for each spectral line, so that the two peaks can be plotted separately. Figure 4-12 shows the resulting focus measure functions for F and F$+\Delta\lambda$ plotted in the same figure for $\Delta\lambda = 10$, 5, 4, 3 and 2 nm. $\Delta\lambda = 4$ nm is where the second peak is zero at the maximum of the first peak. Therefore, 4 nm is the resolution of the spectral imager at F wavelength.

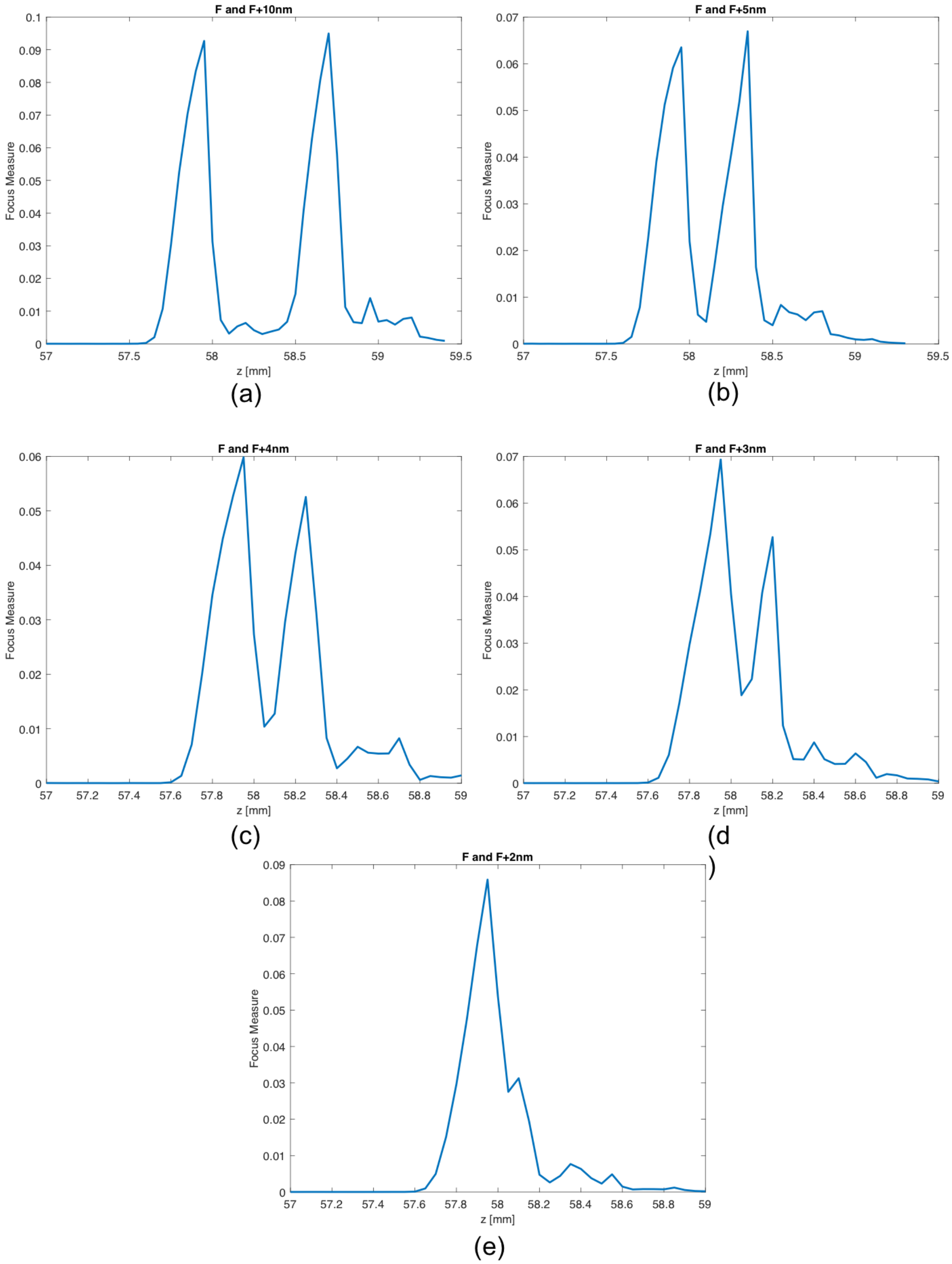

(a)
(b)
(c)
(d
)
(e)

Figure 4-11: Focus measure function plotted versus axial distance for an object with two spectral lines, one at F wavelength and the other one at F+ $\Delta\lambda$. (a) $\Delta\lambda = 10$ nm, (b) $\Delta\lambda = 5$ nm, (c) $\Delta\lambda = 4$ nm, (d) $\Delta\lambda = 3$ nm and (e) $\Delta\lambda = 2$ nm.

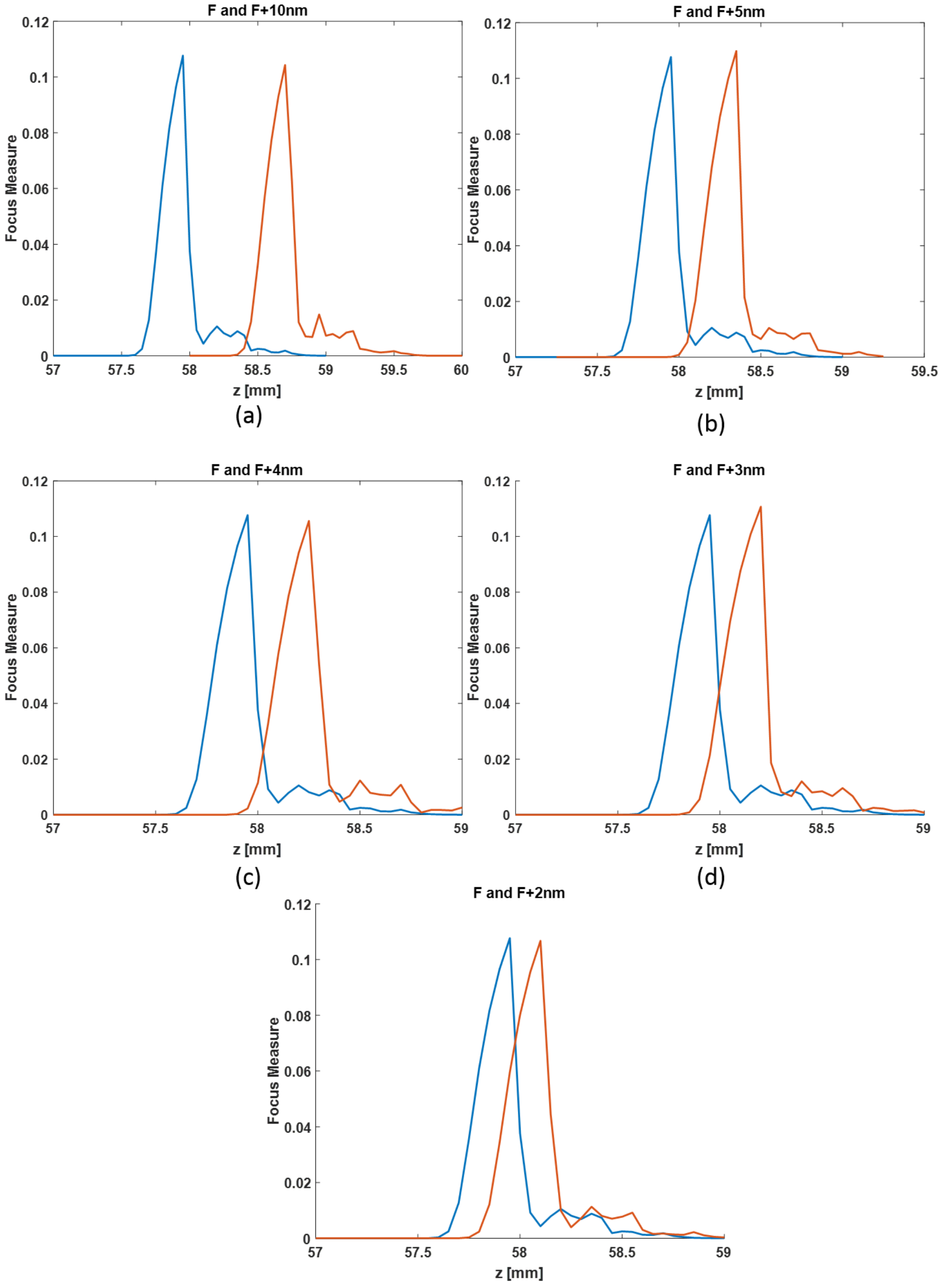

(a)

(b)

(c)

(d)

(e)

Figure 4-12: Focus measure functions for two objects are plotted in the same figure. One object has a single spectral line at F wavelength and the other one has a single spectral line at F+$\Delta\lambda$. (a) $\Delta\lambda = 10$ nm, (b) $\Delta\lambda = 5$ nm, (c) $\Delta\lambda = 4$ nm, (d) $\Delta\lambda = 3$ nm and (e) $\Delta\lambda = 2$ nm.

It must be noted that the resolution would also depend on parameters such as the noise level and the ability of the computational unit to locate the peaks in focus measure function. The calculated 4 nm resolution does not take into account these parameters. To investigate the effect of noise on the spectral resolution, some noise was added to the captured images before feeding them to SFF algorithm. Reference [92] introduces five primary noise sources for a CCD camera: fixed pattern noise, dark current noise, shot noise, amplifier noise and quantization noise. These noise sources are grouped into irradiance-dependent and irradiance-independent sources. and the following noise model of a CCD camera is proposed:

$$I = f(L + n_s + n_c) + n_q \tag{4-11}$$

where I is the observed image brightness, $f(.)$ is the response function of the camera, n_s accounts for all the noise components that are dependent on irradiance L, n_c accounts for the independent noise, and n_q is additional quantization and amplification noise. Similar to assumptions made for noise statistics in [17] and [92], we neglect n_q since most cameras can achieve very low n_q. In addition, we assume n_s and n_c are Gaussian noise with zero mean. The variance of n_s is $L\sigma_s^2$ which is linearly dependent on the irradiance and the variance of n_c is σ_c^2.

Reference [17] defines five different noise levels. These five levels assume incrementing variance values for irradiance-dependent and irradiance-independent noises. The variance values are 0.0005, 0.00176, 0.0032, 0.00429 and 0.0555 for level one through five, respectively. These noises are added to the captured images before SFF algorithm is applied. Figure 4-13 shows the focus measure functions for two spectral lines at F and

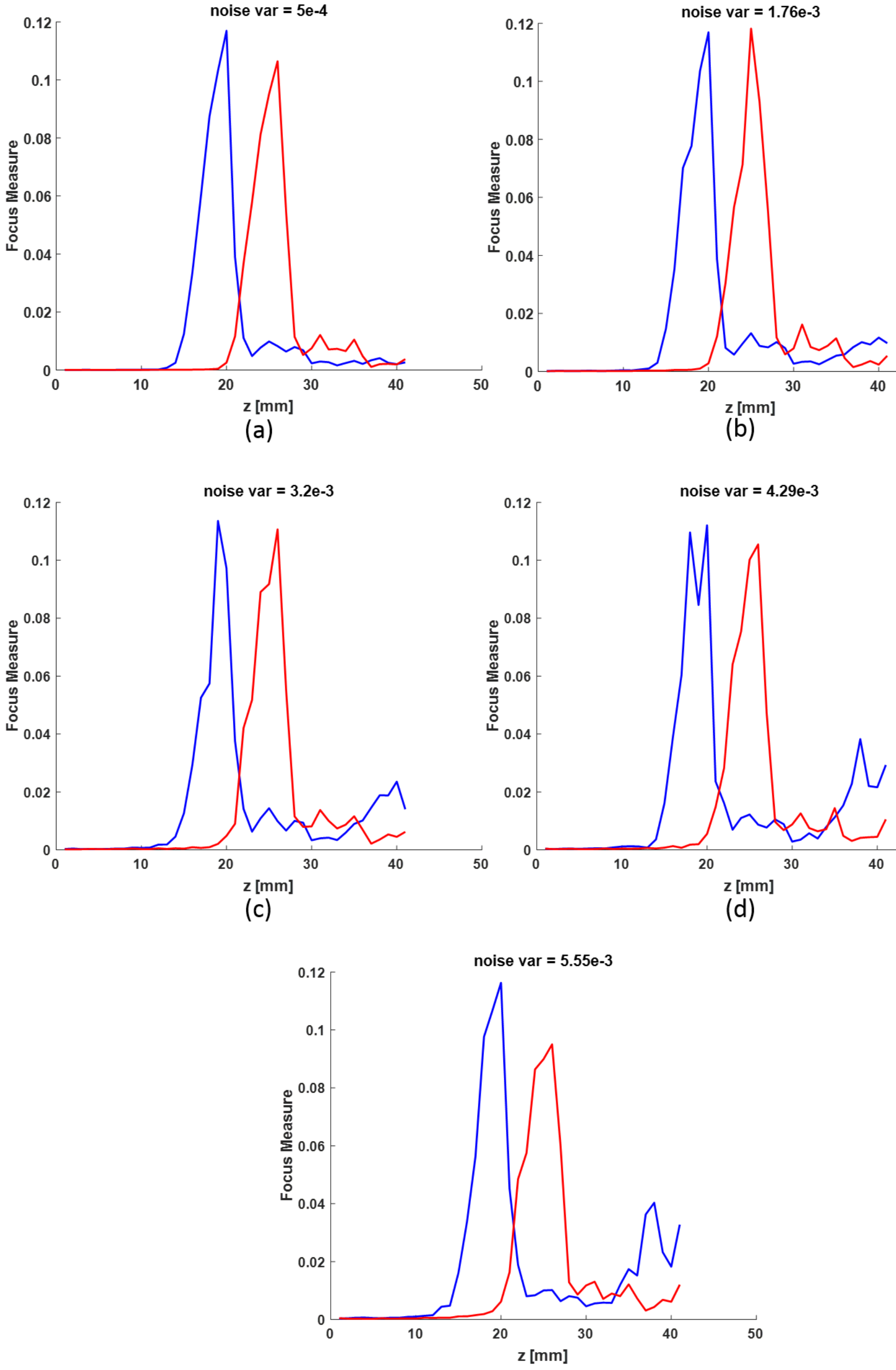

(a) (b) (c) (d) (e)

Figure 4-13: Focus measure function plotted versus axial distance for two spectral lines, one at F wavelength and the other one at F + 4nm. Irradiance-dependent and irradiance-independent Gaussian noises with (a) $\sigma_c^2 = \sigma_s^2 = 0.0005$, (b) $\sigma_c^2 = \sigma_s^2 = 0.00176$, (c) $\sigma_c^2 = \sigma_s^2 = 0.0032$, (d) $\sigma_c^2 = \sigma_s^2 = 0.00429$, (e) $\sigma_c^2 = \sigma_s^2 = 0.00555$, are added to the images before SFF is applied.

F+4 nm to see if the spectral imager can maintain the 4 nm resolution at each noise level. For noise level one to three, the second peak is still zero at the location of first peak and the spectral imager can still resolve the two peaks. For level four and five, the two peaks are not resolvable by the spectral imager anymore.

4.3.2 Second set of simulations

For the second set of simulations, the object is not a point source anymore. Lens system is again used in M = -1 configuration (see Figure 4-5). An object with some spectral content is placed in front of the spectral imager and its image is simulated on a detector with the same size as our CCD. Figure 4-14 (a) shows the object used for the second set of simulations. It is a grid of lines and it contains three different wavelengths. The upper left side of the grid (shown as red) contains C wavelength; the upper right side of the grid (shown as green) contains d wavelength; the lower left side of the grid (shown as blue) contains F wavelength; and the lower right side of the grid (shown as yellow) contains both d and C wavelengths. This object is given as an input to '*Image Simulation'* tool in sequential Zemax. The image plane is moved and at each location an image is produced by the tool. Figure 4-14 (b)-(d) are the captured images at image locations corresponding to F, d and C wavelengths, respectively. It can be seen that the dispersion of the lens system brings each wavelength of the object in focus at a location. Pixels that have F wavelength information (lower left part) are in focus at 57.8 mm away from the last surface of the lens system. The simulated image at this location is shown in Figure 4-14 (b). Pixels that have d wavelength information (upper right and lower right parts) are brought into focus at 63.9 mm away from the lens system. The simulated image at this location is shown in Figure

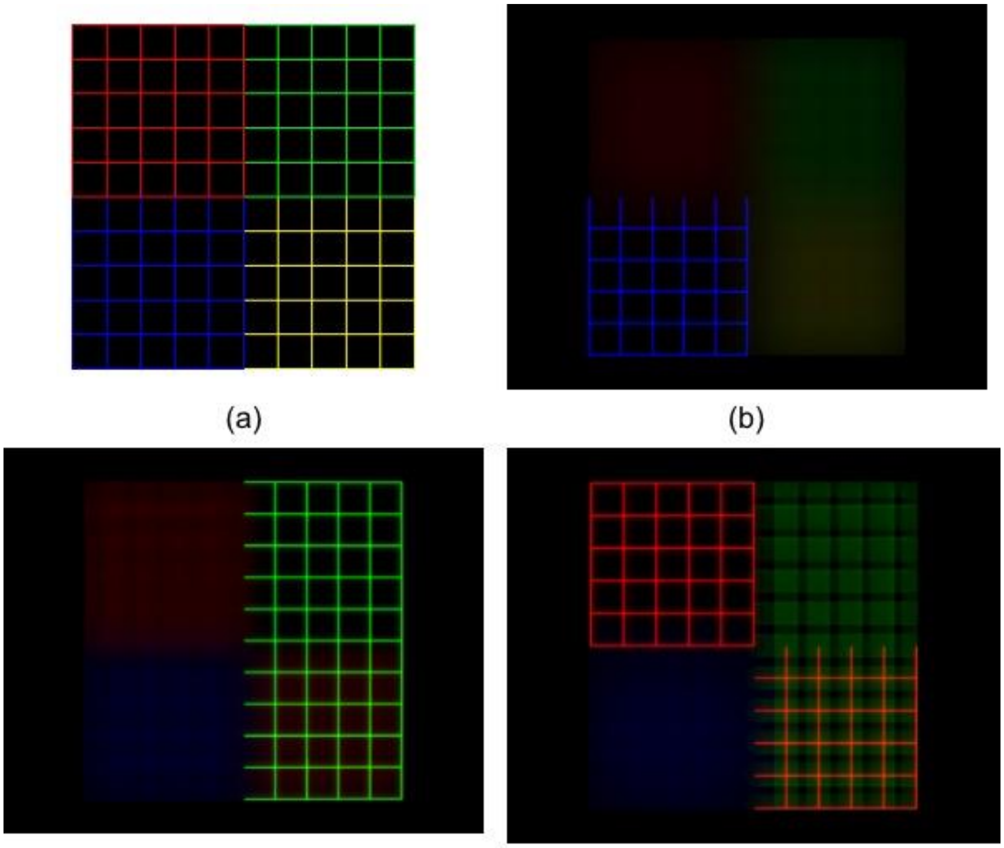

(a) (b)

(c) (d)

Figure 4-14: (a) the object. Blue, green and red pixels have information at F, d and C wavelengths, respectively. Yellow pixels have information at both d and C wavelengths; (b) .; (c) simulated image at image location corresponding to d wavelength and (d) simulated image at image location corresponding to C wavelength.

4-14(c). Finally, pixels that have C wavelength information (upper left and lower right parts) form a focused image at 66.6 mm away from the lens system. The simulated image can be seen in Figure 4-14 (d). Although images in Figure 4-14 are shown in color for clarity, SFF algorithm is applied to grayscale images and the color information is not used by the algorithm. The degree of focus is determined based on the focus measure function value and not based on the color.

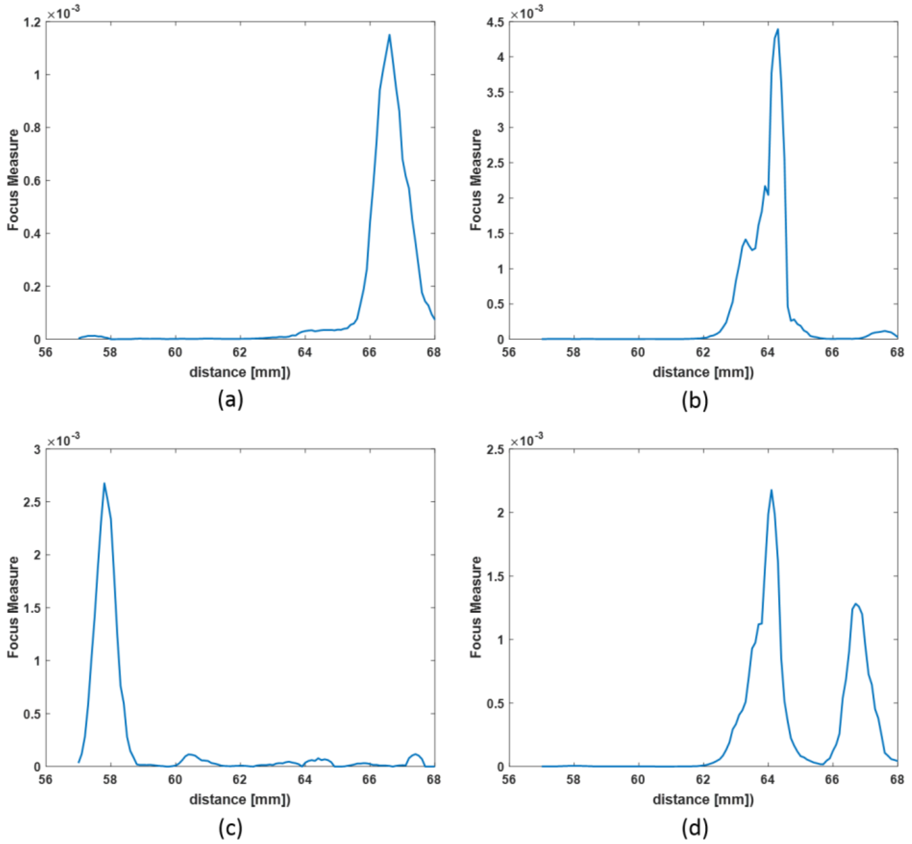

Figure 4-15: Focus measure function versus the distance from the last surface of the lens system for (a) a pixel in upper left side of the object with C wavelength spectral content, (b) a pixel in upper right side of the object with d wavelength spectral content, (c) a pixel in lower left side of the object with F wavelength spectral content and (d) a pixel in lower right side of the object with d and C wavelengths spectral content.

In the second set of simulations, images of the object are simulated at 111 locations in 0.1 mm steps over the distance range of 57 mm to 68 mm from the lens system. The focus measure function introduced in equations (4-8)-(4-10) is applied to every pixel of all these images. To see the behavior of the focus measure function, the function is plotted for four different pixels of the image. Each pixel is in a different quarter of the object with different spectral content. Figure 4-15 (a)-(d) shows these plots. Figure 4-15 (a) is the focus measure function versus distance from the last surface of the lens system for a pixel in upper left side of the object with C wavelength spectral content. Figure 4-15 (b)-(d) are the same plot for pixels in the upper right (d wavelength), the lower left (F wavelength) and the lower right (d and C wavelengths) of the object, respectively. Depending on the spectral content, focus measure function corresponding to each pixel peaks at a specific location. For example, the location of focused image for C wavelength is at distance 66.6 mm. Any pixel that its focus measure function peaks at this distance has spectral content at C wavelength. This occurs for the pixels in the upper left and the lower right quarters of the object. The focus measure plots for two of such pixels are shown in Figure 4-15 (a) and Figure 4-15 (d).

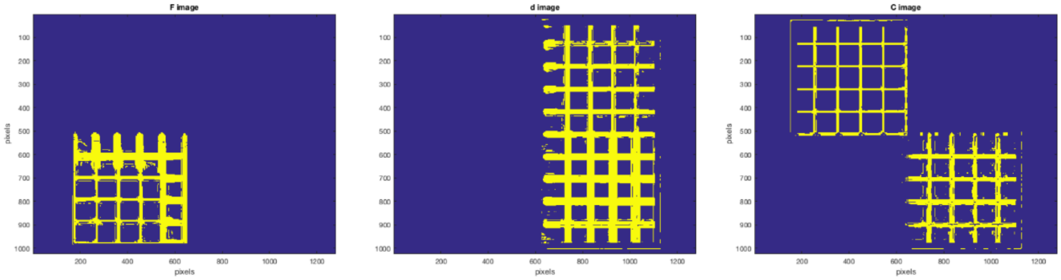

(a) (b) (c)

Figure 4-16: Spectral images of the object shown in Figure 4-14 (a) calculated by SFF algorithm. (a) spectral image at F wavelength, (b) spectral image at d wavelength and (c) spectral image at C wavelength.

By separating the pixels based of where their focus measure functions peaks, spectral images of the object can be calculated. Three spectral images at F, d and C wavelengths are shown in Figure 4-16.

4.4 Experiment results

4.4.1 Implementation and setup

Now that we have designed and simulated our spectral imager, the next step is to build and test it in an experimental setup. We did not want to do a custom-built lens design for our spectral imager for sake of cost and convenience. Therefore, we tried to find a lens system that is made of readily available off-the-shelf lenses and has the closest possible performance to the lens system designed in section 4.1. The result was the lens system shown in Figure 4-17. The lens system consists of three off-the-shelf elements.

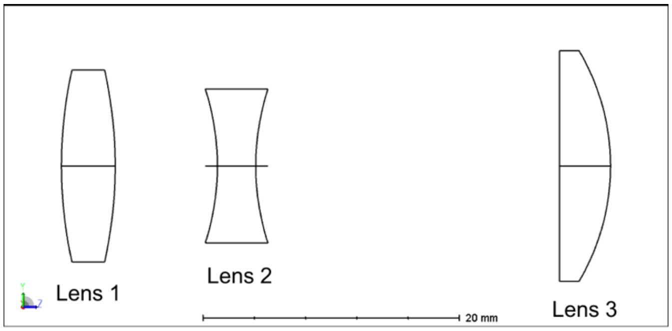

Lens 1	Edmund Optics # 45-101
Lens 2	Edmund Optics # 45-928
Lens 3	Edmund Optics # 49-880

Figure 4-17: The layout of the lens system used in the experimental setup with the list of its off-the-shelf lenses.

Figure 4-18 summarizes a comparison between the specifications of the designed lens system in section 4.1 and the lens system that was used in our experiments. Since we confined ourselves to off-the-shelf lenses, both spatial and spectral resolutions degrade. The RMS spots size increases to 210 microns compared to 46 microns in the designed lens

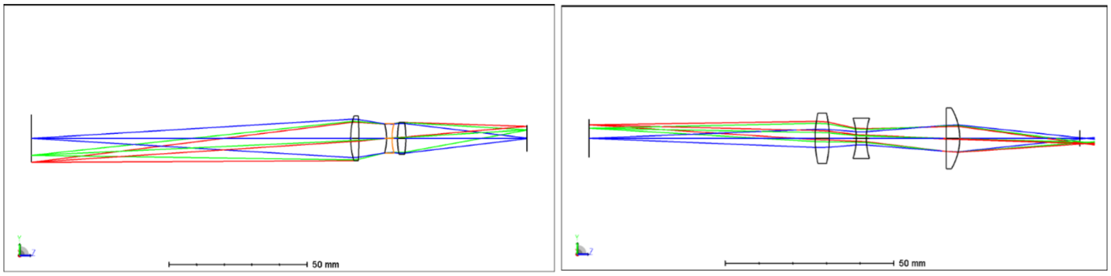

(a) (b)

	(a) designed	(b) setup
magnification @ d wave	M = -0.5	M = -0.4
field of view	13.56 mm x 10.86 mm	16.95 mm x 13.57 mm
object-space NA	0.070	0.124
EFL @F – EFL @C	2.22 mm	0.15 mm
max RMS spot size across the field	46 μm	210 μm

Figure 4-18: Comparison between the designed lens system and the lens design used in the experimental setup.

system which results in lower spatial resolution of the spectral camera. The chromatic aberration is also smaller compared to the originally designed lens system. This results in lower spectral resolution of the spectral camera. EFL is 39.92 mm, 40 mm and 40.07 mm at F, d and C spectral lines. Therefore, the chromatic aberration produced by the lens system separates F and C focal lengths by 0.15 mm compared to 2.22 mm in the design lens system.

Figure 4-19 shows our spectral imaging setup in the lab. A laser projector, projects a pattern with known spectrum on a flat surface. The projected pattern is the object for the spectral imager. We use Microvision SHOWWX laser projector in our setup. The projector contains three laser diodes [93]: an AlGalnP laser diode that lases at 642 nm (red), a frequency-doubled IR laser diode that produce light at 532 nm (green) and a GaN laser diode that lases at 442 nm (blue). There is a lens in front of the projector that focuses the

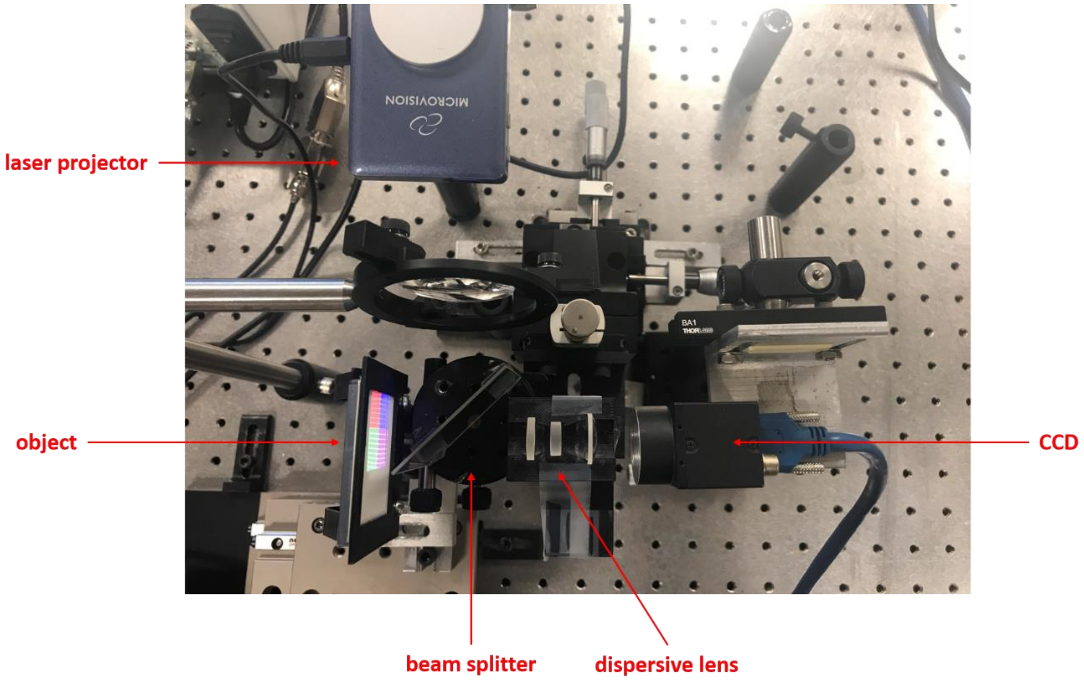

Figure 4-19: Spectral imaging camera setup

projected pattern on the flat surface in front of the camera. Without this lens, the projected lines become too wide by the time they reach the object’s surface.

4.4.2 Results

The projected pattern by the projector is a grid of lines and is shown in Figure 4-20. The green, red and blue lasers inside the laser projector produce the upper-left, upper-right and lower-right sides of the grid, respectively. The lower-left side of the grid is purple and is produced by the combination of the blue and red lasers. The spectral imager detects and differentiates these three wavelengths in the object based on the location where their image is focused and produces the spectral images.

In this setup, the object is mounted on a moving stage and moves to different distances from the lens system. At each location, an image is captured. These images are analyzed

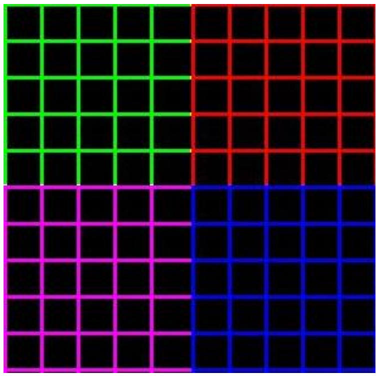

Figure 4-20: The object is created by projecting the shown pattern on a flat surface. The object includes three wavelengths that are the wavelengths of the lasers inside the laser projector.

by SFF algorithm in the computational unit and spectral images are computed based on the location of focused image. The calculated spectral images at the wavelengths of the laser projector's lasers are shown in Figure 4-21.

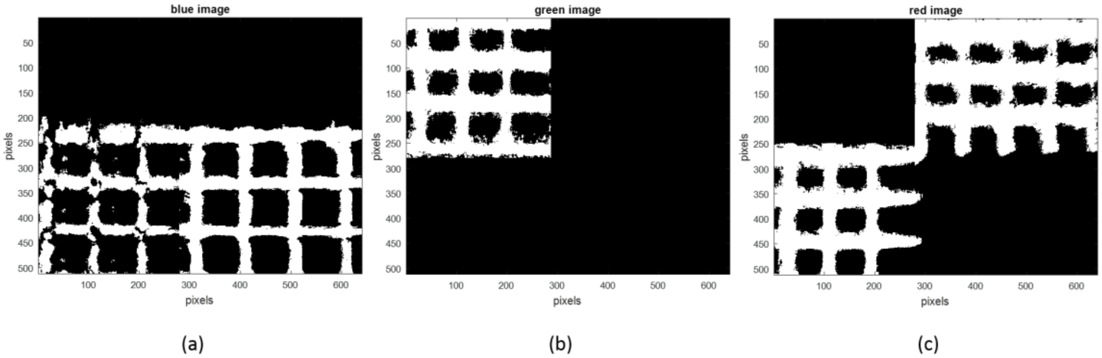

(a)

(b)

(c)

Figure 4-21: Spectral images of the object shown in Figure 4-20 calculated by SFF algorithm. Spectral

As mentioned before, we replaced the optimized lenses in our designed lens system with off-the-shelf lenses for the spectral imager that we used in our experimental setup and as a result of that the resolution of the imager is degraded compared to what we designed and simulated in previous sections. In section 4.3.1, we calculated the resolution of the designed spectral imager to be 4 nm. We did so by introducing two spectral lines in the spectrum of the object and bringing the spectral lines closer together until the spectral imager could not resolve them anymore. In order to calculate the spectral resolution of our spectral imager in the lab setup, we repeated a similar process. Figure 4-22 (a) shows the focus measure function for a blue (442 nm) pixel in the object as a function of axial location. Since our laser projector has three lasers, we know the locations of focused image for three wavelengths that are the wavelengths of the lasers inside the laser projector. We assumed that if we shift the wavelength from 442 nm, which is the wavelength of the blue laser in the laser projector, to 442 nm+$\Delta\lambda$, the focus measure function keeps the same shape as Figure 4-22 (a) but its peak shifts to a different axial location. Figure 4-22 (b) shows these two peaks in one figure, the original peak at 442 nm as well as the shifted peak. Sparrow and Rayleigh criteria are two conventional ways to define the minimum separation of two resolvable Gaussian curves [94, 95]. We use Rayleigh criterion, which is the stricter one between the two. According to this criterion, two symmetrical absorption bands are resolved if the value of the notch between them is less than half of the maximum value. We use the same criterion to define the spectral resolution of the spectral imager that we used in our experimental setup. In order to find the resolution, we shift the blue peak until the notch is less than half of the maximum value. Afterwards, we use equation (4-6) to calculate the spectral resolution. Instead of $\lambda_C - \lambda_F$ we use the wavelengths of the blue and red lasers of the laser projector and instead of $z_C - z_F$ we use the locations of focused image for blue and red lasers of the laser projector. Δz is the minimum axial shift that satisfies the criterion. If we plug these numbers to equation (4-6), we calculate a resolution

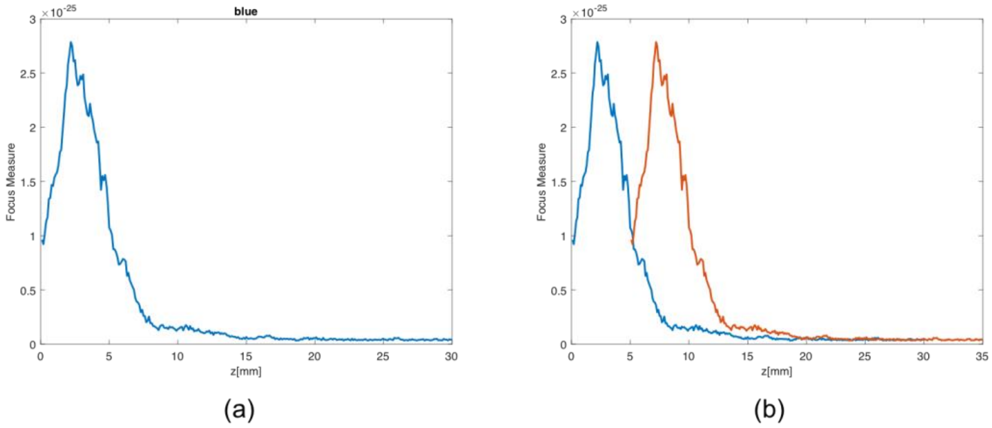

Figure 4-22: (a) Focus measure function for a blue pixel in the image. (b) The blue peak is shifted in z to estimate the spectral resolution of the spectral imager that we have in the setup.

of 40 nm for our spectral imager in the setup. This is consistent with what we should expect considering that the chromatic aberration produced by the lens system used in the setup separates F and C focal lengths by 0.15 mm compared to 2.22 mm in the design lens system (see Figure 4-18 for comparison between the two lens systems).

4.5 Summary

A novel SI technique was introduced in this chapter. This technique uses the chromatic aberration of a lens system to spread the spectral content of the object over a spatial volume. A dispersive lens system with large chromatic aberration was designed for the spectral imager. Images of an object were captured by this lens system and a computational algorithm, called spectrum from focus, was applied in order to calculate the spectral images of the object. Simulation and experimental results of calculating spectral images of objects by the introduced technique were provided.

The designed spectral imaging camera has a spectral resolution of 4 nm and spatial resolution of 46 microns. The effect of noise on the spectral resolution was investigated.

The spectral imager maintains the 4 nm resolution when irradiance-dependent and irradiance-independent Gaussian noises with standard deviation smaller than 0.0032 are added to the captured images before they are analyzed with computational unit. The lens system that we use in our lab setup is made of off-the-shelf lenses and hence has degraded resolution compared to the designed imager. The spatial resolution of the spectral imager that we used in our experimental setup is calculated to be 40 nm.

Spectral and spatial resolutions in this SI system can be improved simultaneously. This is in contrast to conventional SI techniques that offer good resolution in only one of these two domains. Other advantages of the introduced spectral imager are simplicity, being compact and low cost.

CHAPTER 5 : 3D SHAPE MEASUREMENT BASED ON CHROMATIC ABERRATION

This chapter introduces a new optical technique for 3D shape measurement using the spectral imager described in the previous chapter. One of the main objectives of this research is to find a 3D shape measurement technique that does not involve any moving part. Mechanical movement is the limiting factor for speed of measurement in many existing techniques. The introduced technique utilizes the chromatic aberration produced by the dispersive lens system described in Chapter 4 to measure the 3D shape of the object without any moving part.

The introduced technique is especially beneficial in high-volume automated manufacturing and assembly processes where there is a need to detect, in real time, the nonconforming parts that have geometrical dimensions outside of the accepted range of tolerances [10]. Metrology tools are used in these processes for quantification of feature heights, relative angles, radii of curvature, and other metrics that require distance measurements [5]. Due to large number of measurements, the speed of the metrology technique used in such applications is crucial to achievable production rate. The introduced technique requires calibration with a master part whose shape has been measured by another tool and is known to us. After this calibration, the technique measures the 3D shape of subsequent parts.

The idea of using chromatic aberration to eliminate the need for vertical mechanical scan has been employed in chromatic confocal imaging. As discussed in section 2.1.2, chromatic confocal imaging is a non-contact single-point distance measuring technique that benefits from all the advantages offered by confocal imaging such as eliminating the out-of-focus ambient light originated from points on the object other than the one being imaged. Additionally, in contrast to conventional confocal microscopy, chromatic confocal imaging does not require a vertical scan because it uses chromatic aberration of the objective lens to disperse the light vertically. In a chromatic confocal probe, the objective lens of a confocal microscope is replaced by a dispersive lens and a spectrometer is placed behind the confocal pinhole (see Figure 2-2). The wavelength at which the intensity output of the spectrometer peaks can be related to the height of the object at that point. Although due to chromatic coding, no vertical scan is required, but chromatic confocal imaging is a single-point measurement technique and lateral scan of the probe across the surface of the object is still necessary.

The 3D shape measurement technique introduced here does not require any lateral or vertical scan. Similar to chromatic confocal imaging, we make use of chromatic aberration of a lens system to eliminate the vertical scan. For this purpose, we use the dispersive lens system designed in section 4.1. To eliminate the lateral scan, we use active shape from defocus technique discussed in section 2.2.3. Active shape from defocus, contrary to confocal imaging, is an area-measurement technique and therefore does not require a lateral scan to reconstruct the 3D depth map.

As discussed in Chapter 2, passive shape from focus and defocus techniques fail when the object being measured is not textured at all or is weakly textured. For the metrology applications that we are interested in, this is a common case. For this reason, we use an active shape from focus/defocus technique. In other words, we impose some texture onto the object by actively projecting a pattern on it. We image the projected pattern on the object and use that to calculate 3D depth map of the object. Therefore, the object does not need to have a textured surface.

One downside to our active depth measurement technique is that we do not measure the depth at all the points in the field of view of the camera but only at selected points where we are projecting a pattern. As will be discussed later in this chapter, we project a set of parallel stripes and we measure the depth at the object points located at the center of each stripe. In order to increase the density of the calculated depth map, the projected pattern should shift to new positions on the object. Therefore, the number of measured data points in our technique is smaller compared to passive shape from focus and defocus where the depth map of whole object is calculated simultaneously. However, still the number of data points in each measurement is much larger than point-measurement techniques such as confocal or chromatic confocal imaging.

This was mentioned in Chapter 2 but it is worth to point out again that unlike stereo-based approaches, both passive and active shape from focus and defocus techniques use images from a single camera but taken at different focus settings to calculate the depth of the object. Therefore, shape from focus and defocus techniques do not have to solve the issue of correspondence between two images as in stereo. In our introduced depth measurement technique, we make use of the dispersion of the camera’s lens system and change the focus setting by changing the wavelength of the projection without mechanically moving any component. Additionally, in active shape from focus and defocus, the projector and the camera share the same optical axis. Hence, they do not suffer from occlusion and shadowing problems like other active depth measurement techniques where there is an angle between the projector and the camera such as triangulation or structured-light based approaches.

5.1 Methodology

Figure 5-1 illustrates a schematic of the depth measurement technique using the spectral camera described in Chapter 4. We use a laser projector for projection because we need to project the same pattern at two or more different wavelengths with narrow linewidth. The laser projector has three RGB lasers and therefore is capable of projecting at three different well-defined wavelengths. We project a pattern of parallel stripes onto the object at two of these three wavelengths and capture an image at each wavelength. Each projection pattern gets defocused as a function of object’s depth. Additionally, due to dispersion, the lens system has different focal lengths at these two projection wavelengths and the amount of defocus varies between the two captured images. Effectively, by taking advantage of the dispersion of the lens system, we change the focal length of the camera by changing the wavelength of the illumination instead of moving the object or any component of the imaging system. The amount of defocus in the two captured images is used to calculate the depth map of the object.

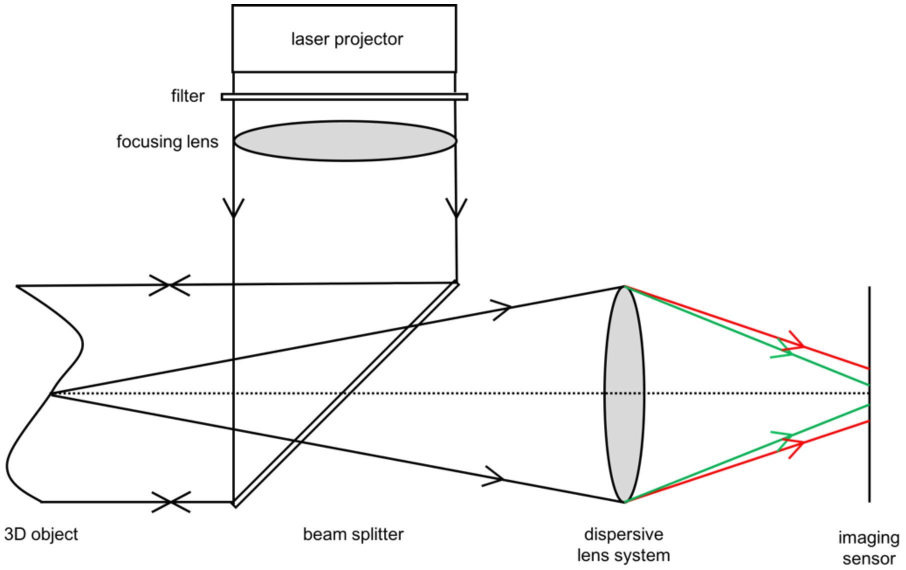

Figure 5-1: Schematic of the novel depth measurement technique using the dispersive lens system designed in section 4.1.

We use Microvision SHOWWX laser projector in our setup. The projector contains three laser diodes [93]: an AlGalnP laser diode that lases at 642 nm (red), a frequency-doubled IR laser diode that provides light at 532 nm (green) and a GaN laser diode that lases at 442 nm (blue). The blue projected pattern from our projector has low and non-uniform intensity. Thus, we use the red and green wavelengths for projection. First, we project a set of stripes on the object at green wavelength of the laser projector and capture an image. Then we project the same pattern at red wavelength of the laser projector and capture a second image. The stripes are blurred as a function of depth of the object. Therefore, the width of the stripes in the image can be related to depth. However, as discussed in section 2.2.2, there is an ambiguity in determining depth from the blur value.

Two depths, one behind and one in front of the location of focused image, result in the same blur value. At least two images are required to address this ambiguity.

We also added a bandpass filter in front of the projector to make sure that the projection contains a single wavelength. This is because even when we are projecting at a single wavelength, the other lasers of our projector do not turn off completely. Therefore, we had to place a green filter in front of the projector when projecting at green and replace it with a red filter when projecting at red.

We also added a lens in front of the projector to focus the stripes on the object. The beams of the laser diodes are propagating with some diverging angle. Without the lens, the stripes become large when they reach the object. This would limit the number of stripes and as a result the number of depth measurements in each projection. The role of the lens is to focus the beam at the location of the object. We are assuming that the depth of field of the beam is large at the location of the object and does not change significantly over the range of measurement. This assumption is to make sure that the width of the projected stripes remains the same for different depths of the object and any change in the width of the imaged stripes is due to depth changes and not because of change in the projected beam size. As it will be discussed later, our depth calculation method involves a calibration process. Therefore, even if the assumption of constant beam size is not strictly valid, the calibration process will include the change of beam size for different depths of the object and accounts for that in calculating depth.

5.2 Pre-processing of the images

Before the captured images are used to calculate the degree of defocus, there are some pre-processing steps. First step is to reduce the noise in captured images. To that end, at each wavelength of illumination we capture three images instead of one and average them to obtain a single image. In addition, we apply a Gaussian filter on the image and we will see later that this filtering step helps to obtain smoother and less noisy results when calculating defocus value of each stripe. The standard deviation of the Gaussian filter in frequency domain is 20 mm^{-1}.

Magnification correction is the second step. The focal length and consequently the magnification of the dispersive lens system varies with wavelength. In order to make sure that two captured images under red and green projection capture the same area of the object, we need to compensate for magnification variation. For two images captured at the same location but one at red and one at green wavelength, the red one has the larger magnification and thus the camera images smaller area of the object. This is because the focal length of the dispersive lens system is larger at red compared to green. After we capture two images of the object at two different wavelengths of projection, we select the red image as the reference image and scale the green image to show the same area of the object as the reference image. Matlab’s intensity-based image registration function, *imregister*, is used to scale the green image.

After projecting the pattern at two different wavelengths, capturing two images each at one wavelength, and doing the pre-processing steps, now we need to measure the spread of each stripe at all points along the stripe in each captured image. This will be discussed next.

5.3 Calculating the degree of defocus of imaged stripes

The projected parallel stripes are imaged by the dispersive camera on a fixed CCD. The stripes are defocused in the image based on the distance of the object from the camera or in other words, based on the distance of the CCD from the location of focused image. Hence, the spread of stripes contains information about the depth of the object. We need to calculate the local width of each stripe along its length and use that to calculate depth.

We investigated different methods for measuring the local width of the stripe at each pixel across the stripe. Girod and Scherock [96] assume a Gaussian distribution for the intensity across the width of the blurred line and take the standard deviation of the Gaussian as the width of the line. They take the intensity in the direction perpendicular to the line and remove the DC bias. Following equation is used to calculate the standard deviation:

$$\sigma_{stripe} = \sqrt{\frac{\int x^2 I(x)dx - \left(\int xI(x)dx\right)^2}{\int I(x)dx}} \tag{5-1}$$

where σ_{stripe} is the estimation of the width of the stripe, x is the direction perpendicular to the stripe and $I(x)$ is the intensity after removing the DC bias. The range over which the integrals are calculated is approximated to be the mid-points in between the defocused stripes in the image.

Pentland et al. [34] assume that stripes have zero width when in focus and blur into a stripe with uniform intensity within a radius and zero intensity outside that radius, when out of focus. The width of the blurred stripe is equal to radius of geometrical optics circle of confusion. With these assumptions, the energy or the integral of intensity squared of the stripe is proportional to width of the stripe. They take the intensity at the cross section of the stripe at each point across the stripe. Then they subtract the DC bias from the intensity function and normalize it to unit area. After removing the DC bias and normalizing to unit area, the relation between the integral of intensity squared and the width of the stripe is as follows:

$$E = \int_{-r_c}^{r_c} I^2(x)dx = \frac{16}{3\pi^2} r_c \tag{5-2}$$

where E is the integral of intensity squared, x is the direction perpendicular to the stripe, $I(x)$ is the intensity after removing the DC bias and normalizing to unit area, r_c is the radius of circle of confusion which is the estimate of the width of the stripe.

In order to calculate E and subsequently r_c, the authors assume the boundaries of the integral in equation (5-2) to be the maximum value that r_c can take in the range of measurement (r_{max}) and calculate an estimation of E from the following equation:

$$E \approx \int_{-r_{max}}^{r_{max}} I^2(x)dx = \frac{16}{3\pi^2} r_c \tag{5-3}$$

The estimated value of E is proportional to r_c that is the estimation of the width of the stripe.

We found the widths calculated from both equation (5-1) and (5-3) to be susceptible to noise. These methods assume that the intensity of the line goes to zeros after some distance from the center of the stripe. In reality, the intensity does not go to zeros because of the ambient light and other sources of noise. Calculating the DC bias, determining the range over which the integrals are calculated and normalizing to unit integral over that range are the factors that are affected by noise. These factors make the widths calculated from (5-1) and (5-3) sensitive to noise.

Lertrusdachaku et al. [39] fit a Gaussian function to the intensity in the direction normal to the line and choose the standard deviation of the fitted Gaussian to be the width of the line. However, the fitting process makes the algorithm slow. We are interested in faster and less computationally intensive ways to calculate the width of each stripe in the image.

The approach that we take here is that after pre-processing of the images, we subtract the intensity of the darkest pixel in the image, i.e. the pixel with smallest intensity, from the whole image. We take the intensity in the direction perpendicular to the stripe over the distance in between two adjacent stripes. We find the maximum value of intensity and find the two points that their intensity is equal to $\exp(-0.5)$ times the maximum. We choose this value to be twice the width of the stripe (see Figure 5-2). For a perfect Gaussian, the intensity drops to $\exp(-0.5)$ times the maximum at a $\pm\sigma$ distance from the center (σ is the standard deviation). This process is repeated for every pixel across the stripe in the image.

When applying the above method, we need to find the maximum of the signal and the points where the intensity decreases to $\exp(-0.5)$ times the maximum. Therefore, we are using the intensity values only at locations where the signal is strong and signal to noise ratio is large. The method that we use here does not use the signal values at the tails of the Gaussian where the intensity of the signal and hence the signal to noise ratio is small. Despite the fact that we still need to remove the DC bias by subtracting the minimum intensity of the image, we found this method to be less sensitive to noise than equation (5-1) and (5-3).

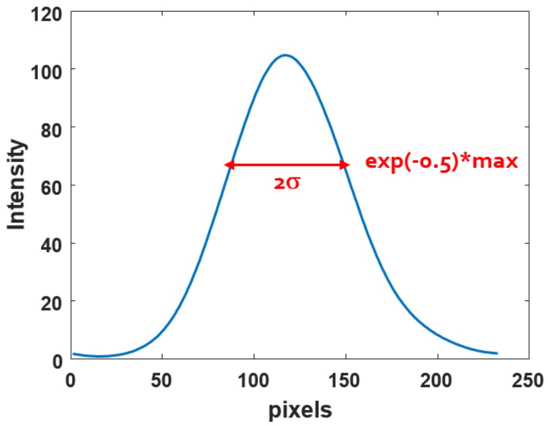

Figure 5-2: To calculate the degree of defocus, we find the points where the intensity drops to $\exp(-0.5)$ times the maximum intensity. We take the half of the distance between these two points as the spread of the stripe.

Once the width of the stripe is calculated for all the pixels along the stripe, the next step is to measure depth based on the calculated widths. We do that through a calibration process that is explained in the following section.

5.4 Coarse calibration

After measuring the spread of projected stripes in captured images, we need to calculate depth based on the measured defocus of the stripes. This is done through a coarse calibration process that provides a transformation from blur size to depth. During this process we use a flat surface as our object as illustrated in Figure 5-3. We project the stripes on the flat at green and red wavelengths of the laser projector. We move the flat surface in small steps to different distances from the lens system within the range of measurement. At each position, we capture images of the stripes projected on the flat object and measure their spread for all the pixels along the stripes. Since the defocus values are calculated at known depths, we obtain defocus values as a function of depth for each wavelength and for every pixel on the stripes.

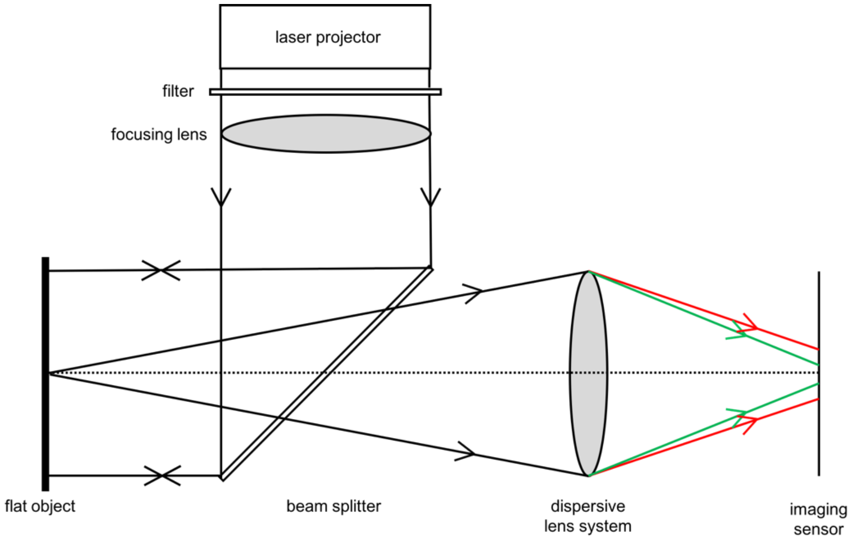

Figure 5-3: Schematic of the calibration process.

Figure 5-4 shows two sample images captured during calibration. Both images were taken at the same location but at different wavelengths. Please note that in ideal situation where there is no aberration in the lens system, the object is perfectly flat, and the projected stripes maintain the same width in the range of measurement for both wavelengths, we do not need to measure the defocus for all pixels during calibration process. They all should be defocused with the same degree for a flat surface. However, the aberration of the imaging lens system as well as the lens in front of the projector will cause the stripes in the image to have different widths even when captured from a flat surface. Additionally, as discussed previously, the Gaussian beam size of the lasers in the projector changes as a function of

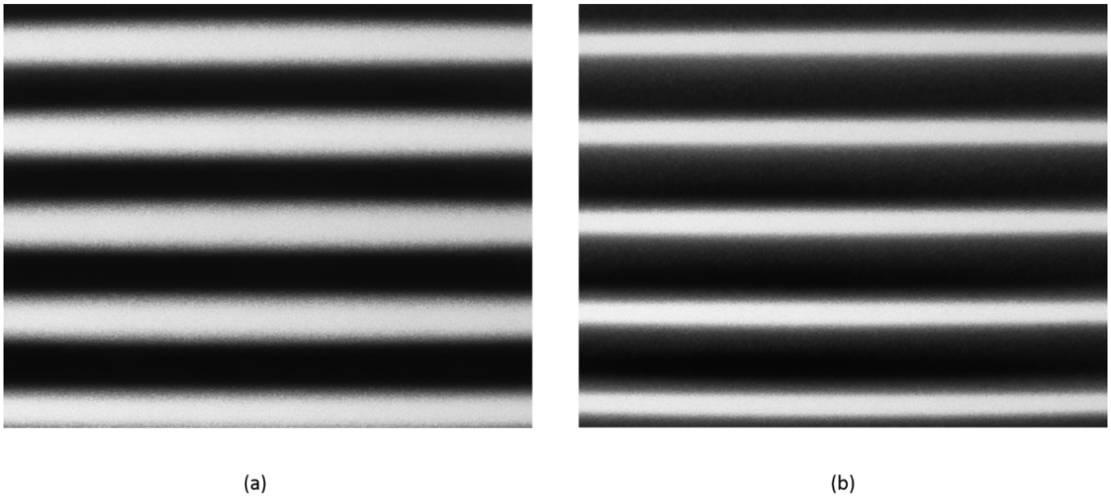

Figure 5-4: Two sample images captured during calibration. Both images were taken at the same location but at different wavelengths: (a) red (b) green

distance from the projector and laser properties such as wavelength. The calibration process takes into account all these factors. Because of all these effects, we measure the red and green defocus for all pixels in the image during this calibration process and obtain defocus values as a function of depth for each pixel individually. Later, when calculating depth based on defocus values measured during calibration, we refer to the values corresponding to each pixel separately and calculate the depth based on those values.

We used a thick paper attached to a mirror as our flat. Paper is considered flat within the depth resolution that our depth measurement technique has. The flat object is mounted on a moving stage. At each location and for each wavelength, an image is captured. The defocus values are measured for all the captured images. Figure 5-5 shows samples of the calculated red and green defocus values versus depth for a single pixel. Similar plots are obtained during the coarse calibration for all pixels along the stripes. The flat object moves in 50 microns steps. The plots include the originally measured defocus values (blue curve) as well as a smoothed version of the same curves (red curve).

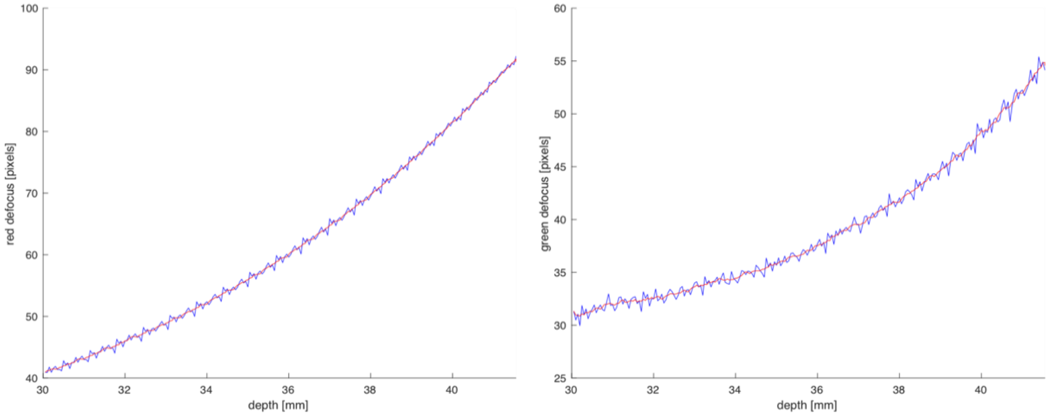

(a) (b)

Figure 5-5: Defocus values versus depth for a single pixel, calculated during calibration for (a) red (b) green projection. The figure shows the originally calculated curves (plotted in blue) as well as a smoothed version of the curves (plotted in red).

5.5 Depth calculation

After projecting a set of parallel stripes on the object at two different wavelengths and measuring how much the stripes are defocused in captured images, we search the measured defocus values in the coarse calibration process to see which depth gives the same red and green defocus values. During coarse calibration, we obtain depth as a function of green and red defocus for each pixel along the stripes. We fit a 2D function to calibrated depth values versus red and green defocus values at each pixel. This fitting is only done once in calibration process and is not repeated during measurement. During the measurement, when two defocus values are calculated for a pixel, we feed these defocus values to the fitted function for the same pixel from calibration process. The fitted function gives us the depth that best fits the calculated red and green defocus values at that pixel.

5.6 Fine calibration

A coarse calibration process was performed on a flat object, as described in section 5.4, in order to transform calculated defocus values to depth values. However, as will be discussed in this section, geometrical features of the object such as the slope of object's surface or existence of the sharp ridges affect the measured defocus values. Consequently, our form measurement technique requires another calibration process performed on a master part with the same geometrical properties as the objects that will be measured by this technique. Therefore, for each object shape that is being measured by this technique, we need a reference part whose depth is measured and known by another technique. During the fine calibration process, we calibrate depth values calculated by our technique with the known form of this reference part and calculate a correction vector based on that. Then we apply this correction vector to all objects measured afterwards.

Figure 5-2 shows a sample intensity plot of the imaged stripes over a cross section of the stripe and section 5.3 describes how we calculate the defocus value from this plot. If the intensity follows the Gaussian format of:

$$I(x) = Aexp(-\frac{x^2}{2\sigma^2}) \tag{5-4}$$

where x is the direction normal to the stripe, A is the amplitude of the function and σ is the estimate of the defocus, then the separation between two points where the intensity drops to $\exp(-0.5)$ of the maximum is equal to 2σ. In reality, equation (5-4) has a DC component that comes from ambient light and other sources of noise. We subtract the intensity of darkest point of the object from the signal before we calculate equation (5-4) from above method to reduce the ambient factor. However, a DC component still remains in the intensity. This DC component has to be small compared to the signal in order for the σ calculation method to remain accurate. The intensity in the direction normal to the line with the DC component added has the following format:

$$I(x) = Aexp\left(-\frac{x^2}{2\sigma^2}\right) + B \qquad (5\text{-}5)$$

where B is the DC component.

The geometry of the object affects the σ calculation too. One effect is that the slope of the object and the angle that the normal to the surface makes with the optical axis of the lens system, determines the amount of light collected by the lens from a measurement point. Therefore, A in equation (5-4) depends on the local slope of the object. However, despite this, the separation between two points where the intensity drops to $\exp(-0.5)$ of the maximum, is still equal to 2σ independent of A assuming that B is negligible. The second effect of object geometry on σ calculation is that due to spot size or lateral resolution of the lens system, light from an area and not a single point of the object reaches each measurement point in the image. In other words, each measurement point sees an integral of Gaussian functions coming from points within object-space lateral resolution of the lens system. These points have different heights and consequently cause different defocus values. This means that instead of equation (5-4), the cross-sectional intensity at each measurement point is the sum of Gaussian functions:

$$I(x) = \int \{A(y')exp\left(-\frac{x^2}{2\sigma(y')^2}\right) + B(y')\}dy' \tag{5-6}$$

The integral is over all points of the object that are imaged at the position of the stripe where the cross section is being calculated. This effect can be minimized by using a lens system with small lateral resolution. For the lens system that we use in our setup, the maximum spot size across the field of view is $210\ \mu m$ (see Figure 4-18). The larger is the height difference within the lateral resolution of the lens system, the more significant is this effect.

Since the calculated defocus value depends on the geometry of the object, our technique requires a calibration process performed on an object with similar geometry to the objects that this technique will be applied to. We call this second calibration step, fine calibration. We apply our measurement technique to a reference part that its 3D depth map is known from some other measurement technique. We calculate a correction factor for each measurement point so that after applying this correction factor, our measurement matches the known depth of the reference part. We apply the same correction factor to all the following measurements.

The degree of similarity between the reference part and the part being measured would influence the effectiveness of this calibration process. The alignment of the reference part with respect to the lens system compared to the alignment of the part being measured is another influential factor. When there is a discrepancy between the alignment of the reference part and the alignment of the object being measured, the camera sees different geometrical features such as slope. This would reduce the effectiveness of the fine calibration process and results in larger errors.

5.7 Results

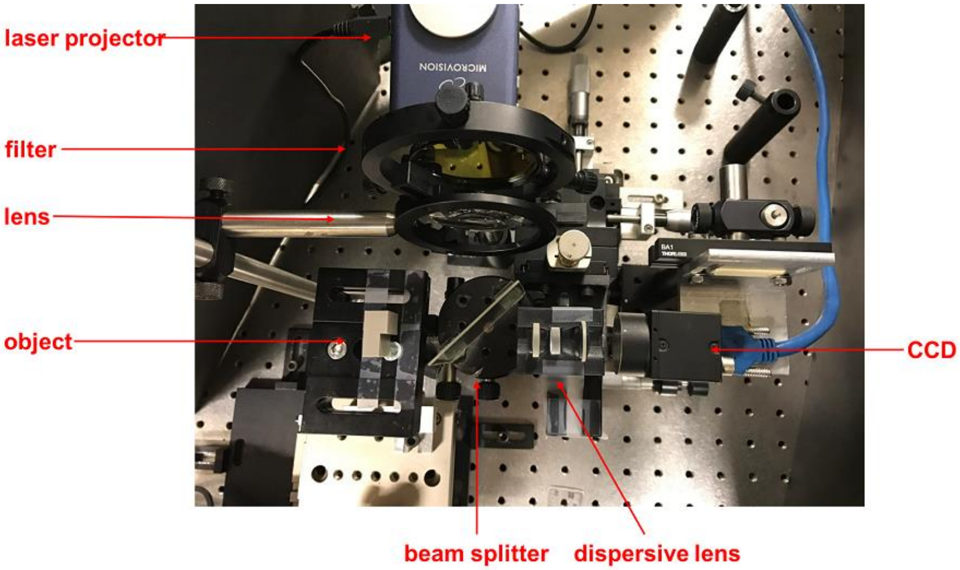

Figure 5-6: The experimental setup used for 3D shape measurement.

Figure 5-6 shows our setup in the lab. The laser projector, filter, focusing lens, beam splitter, dispersive lens, CCD and object are all marked in the picture. We measured two objects in this setup: a 135-degree wedge and a section of a cylinder with 11.73 mm radius. Figure 5-7 shows a cross section of these two objects. We made the objects with a 3D printer and measured the 3D shape along three projected stripes with our technique in the setup shown in Figure 5-6. We also measured these two objects with a Mahr stylus profilometer for comparison.

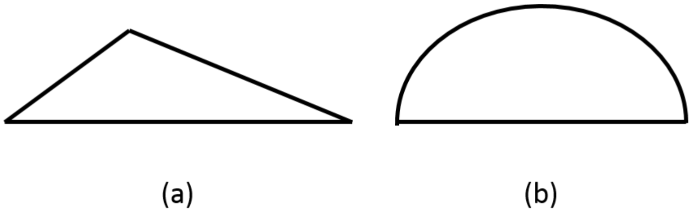

Figure 5-7: Schematics of the cross sections of the two objects that we measured in our setup (a) a 135-degree wedge and (b) a section of a cylinder with 11.73 mm radius.

Figure 5-8 shows the results of measuring the wedge with our depth measurement technique. Figure 5-8 (a) and (b) are the images captured under red and green projection. The stripes are defocused based on the 3D shape of the object that in this case is a wedge. It can also be seen that the degree of defocus is different for red and green images as a result of chromatic aberration of the lens. Figure 5-8 (c) and (d) show the calculated degree of defocus by method explained in section 5.3 for pixels along one of the projected stripes Figure 5-8 (c) is the degree of defocus for red image and Figure 5-8 (d) is the degree of defocus for green image for pixels along the same stripe. Figure 5-8 (e) shows the depth calculated from the red and green defocus values after referring to the calculated defocus values during coarse calibration. Blue is the measured depth after coarse calibration process and red is the measured depth values by the profilometer. During the fine calibration process, we define a correction factor for each pixel of the stripe that matches our measurement with the reference measurement from the profilometer. Figure 5-8 (e) shows the result after fine calibration.

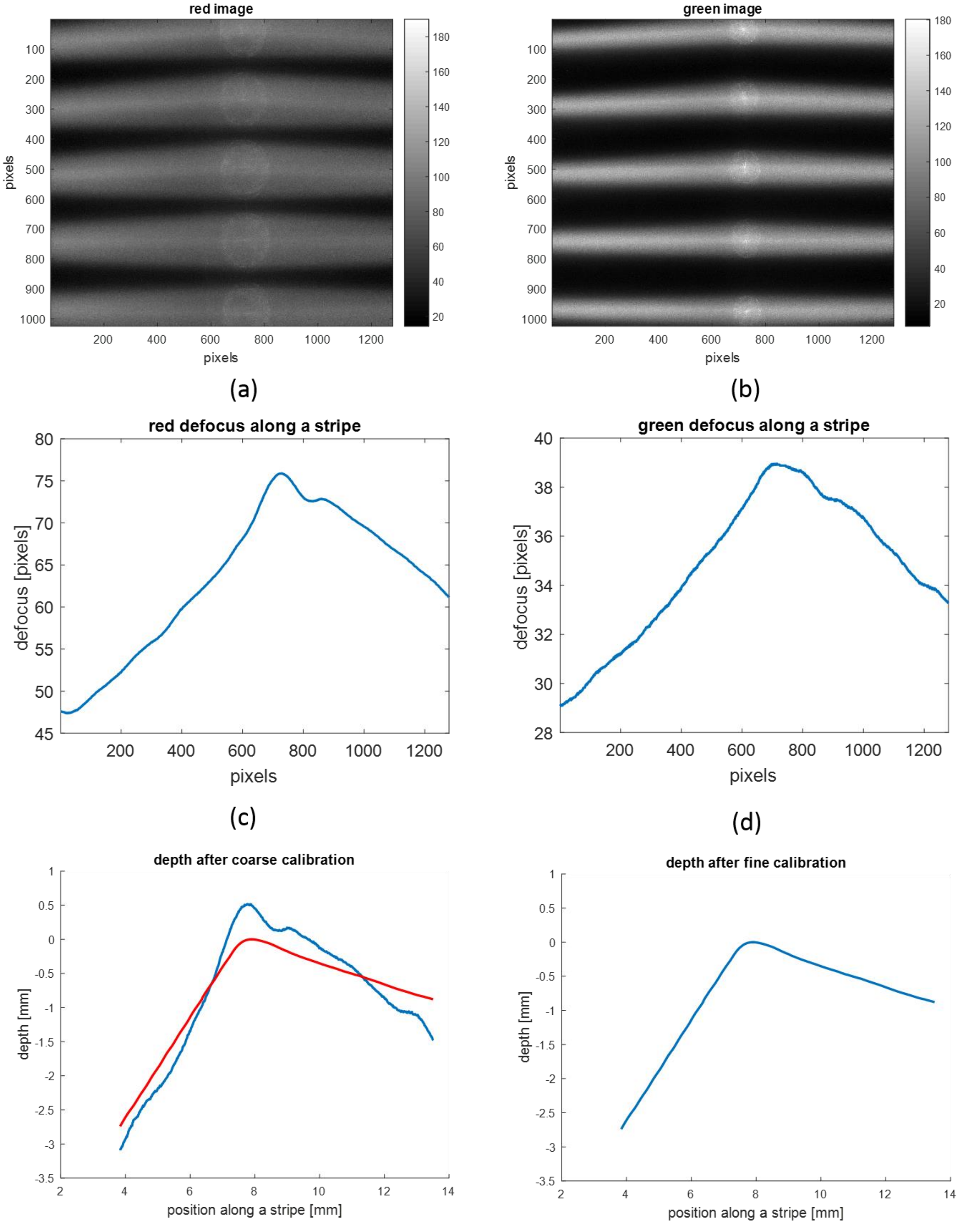

(a) (b) (c) (d) (e) (f)

Figure 5-8: Measuring a wedge with our depth measurement technique. (a) image captured under red projection, (b) image under green projection, (c) red defocus for pixels along one selected stripe, (d) green defocus for pixels along one selected stripe, (e) depth measured from red and green defocus along a stripe after coarse calibration and (f) measured depth along a stripe after fine calibration. Blue is the measured values by our technique and red is the measured depth values by the profilometer.

We repeated the measurement process ten times in a row on three projected stripes. Figure 5-9 shows all the ten measurements along the first projected stripe plotted in the same figure with ten different colors. The standard deviation of these ten measurements averaged over all the pixels on one stripe is 10.9 microns. Figure 5-10 shows a plot of standard deviation values along the first projected stripe. Figure 5-11 shows ten measurements along the second projected stripe and Figure 5-12 is the plot of corresponding standard deviation values. The average standard deviation is 11.4 micron along the second projected stripe. Figure 5-13 and Figure 5-14 show the result of measurement along the third projected stripe. The average standard deviation of ten measurements along the third stripe is 13.0 micron.

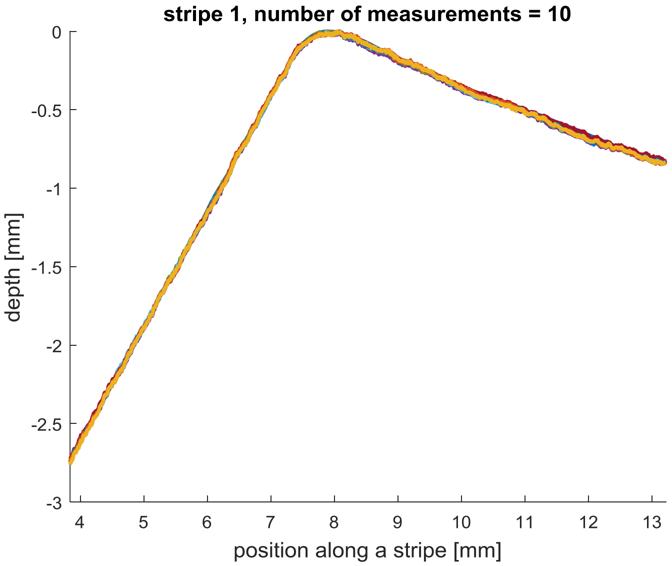

Figure 5-9: Depth along the first projected stripe on the wedge was measured ten times in a row. All ten measurements all plotted in the same graph in ten different colors. The standard deviation of these ten measurements averaged over all the pixels on one stripe is 10.9 microns.

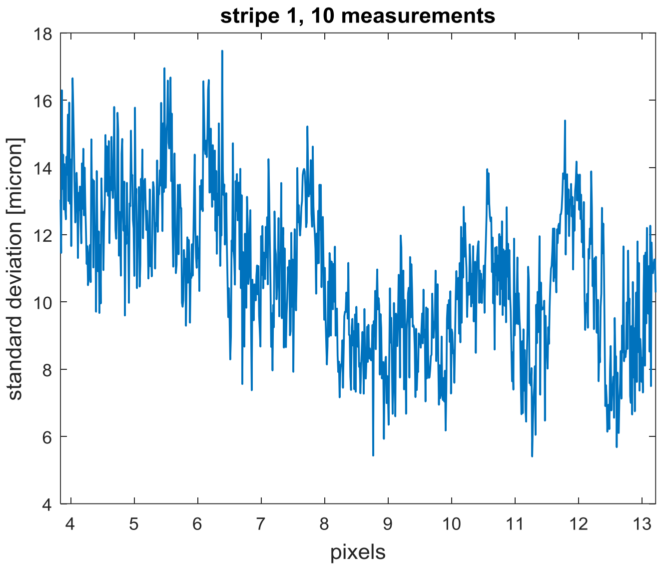

Figure 5-10: The standard deviation of ten subsequent measurements of the wedge along the first projected stripe.

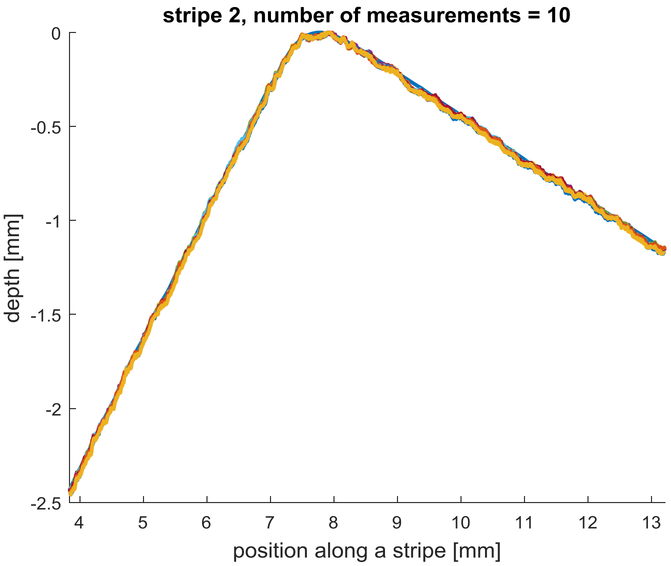

Figure 5-11: Depth along the second projected stripe on the wedge was measured ten times in a row. All ten measurements all plotted in the same graph in ten different colors. The standard deviation of these ten measurements averaged over all the pixels on one stripe is 11.4 microns.

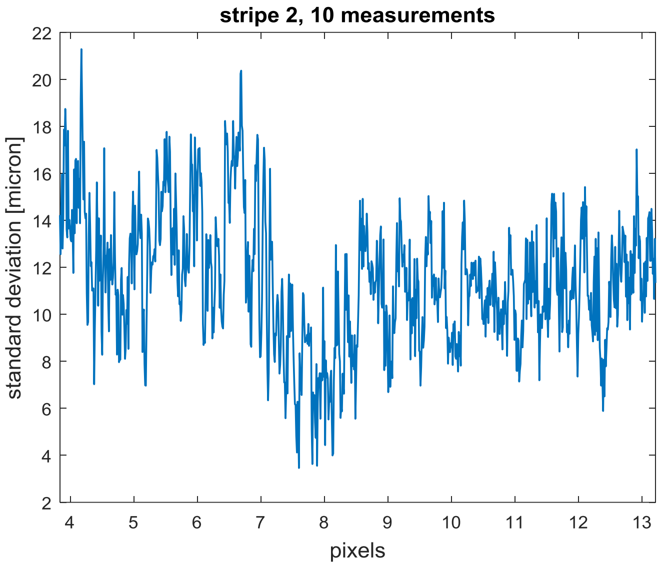

Figure 5-12: The standard deviation of ten subsequent measurements of the wedge along the second projected stripe.

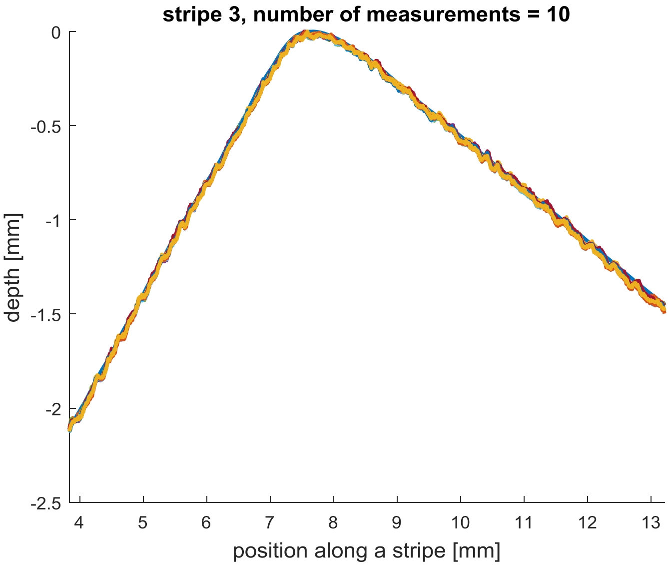

Figure 5-13: Depth along the third projected stripe on the wedge was measured ten times in a row. All ten measurements all plotted in the same graph in ten different colors. The standard deviation of these ten measurements averaged over all the pixels on one stripe is 13.0 microns.

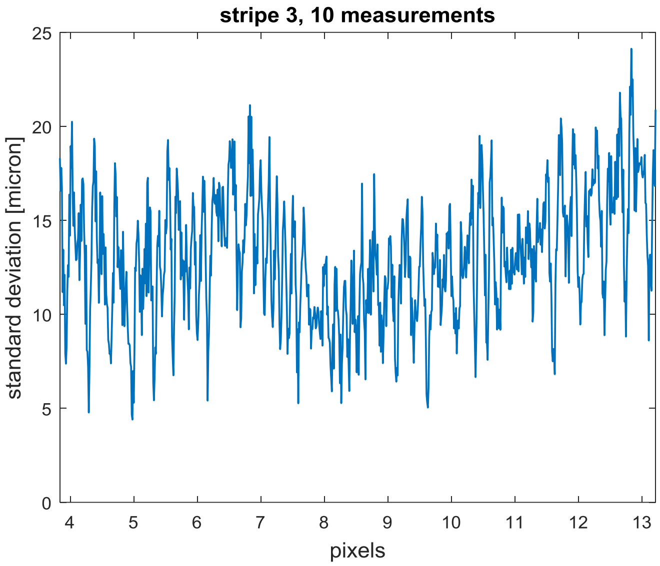

Figure 5-14: The standard deviation of ten subsequent measurements of the wedge along the second projected stripe.

We measured the cylinder with our technique too. Figure 5-15 to Figure 5-21 demonstrate the results. The average standard deviation of ten measurements along the first, second and third projected stripes are 13.1 micron, 8.6 micron and 8.3 micron, respectively.

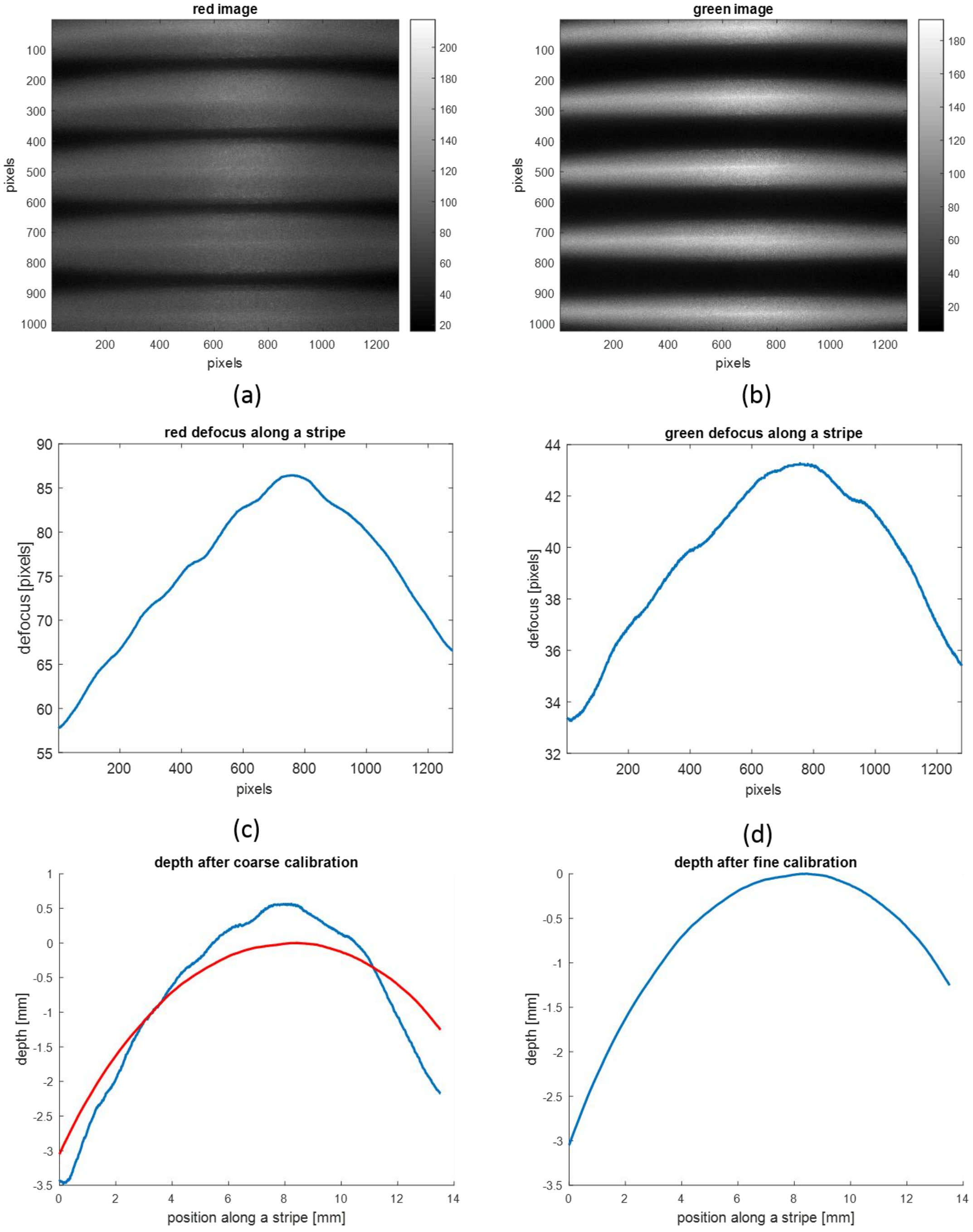

(a) (b) (c) (d) (e) (f)

Figure 5-15: Measuring a section of a cylinder with our depth measurement technique. (a) image captured under red projection, (b) image under green projection, (c) red defocus for pixels along one selected stripe, (d) green defocus for pixels along one selected stripe, (e) depth measured from red and green defocus along a stripe after coarse calibration and (f) measured depth along a stripe after fine calibration. Blue is the measured values by our technique and red is the measured depth values by the profilometer.

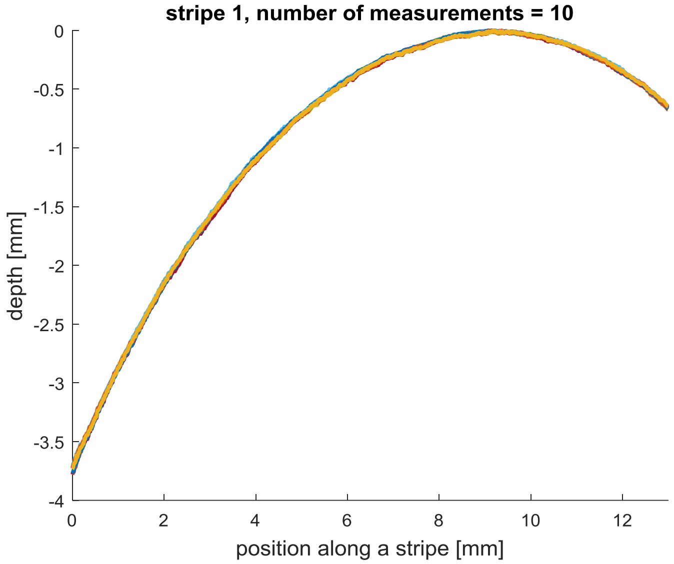

Figure 5-16: Depth along the first projected stripe on the cylinder was measured ten times in a row. All ten measurements all plotted in the same graph in ten different colors. The standard deviation of these ten measurements averaged over all the pixels on one stripe is 13.1 microns.

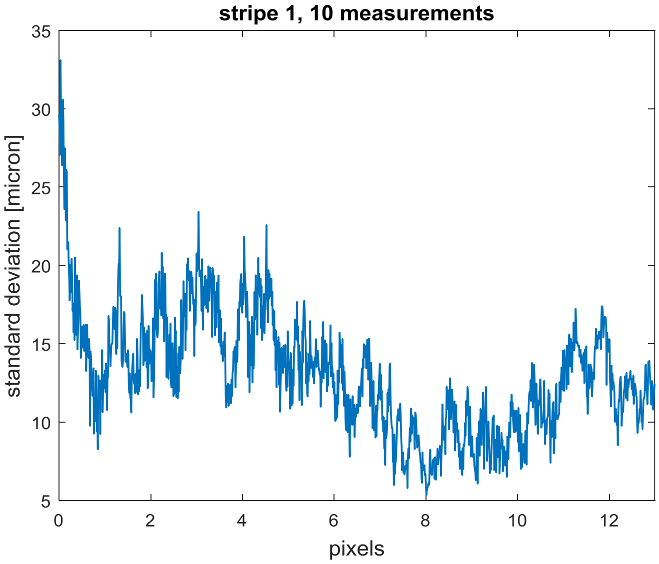

Figure 5-17: The standard deviation of ten subsequent measurements of the cylinder along the first projected stripe.

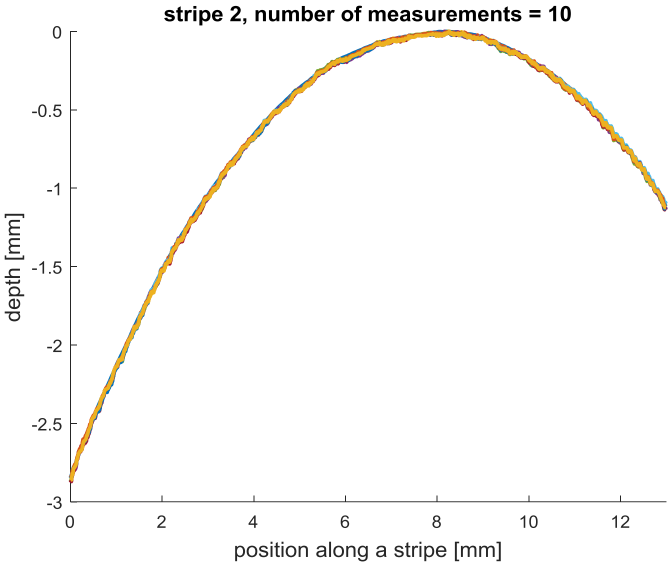

Figure 5-18: Depth along the second projected stripe on the cylinder was measured ten times in a row. All ten measurements all plotted in the same graph in ten different colors. The standard deviation of these ten measurements averaged over all the pixels on one stripe is 8.6 microns.

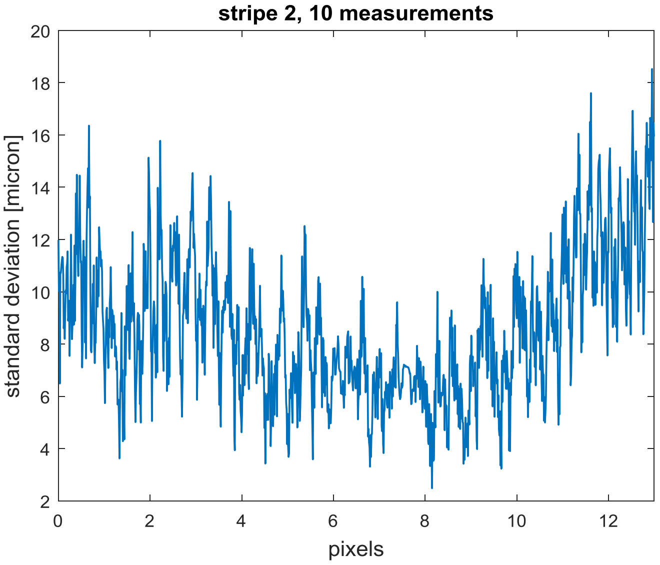

Figure 5-19: The standard deviation of ten subsequent measurements of the cylinder along the second projected stripe.

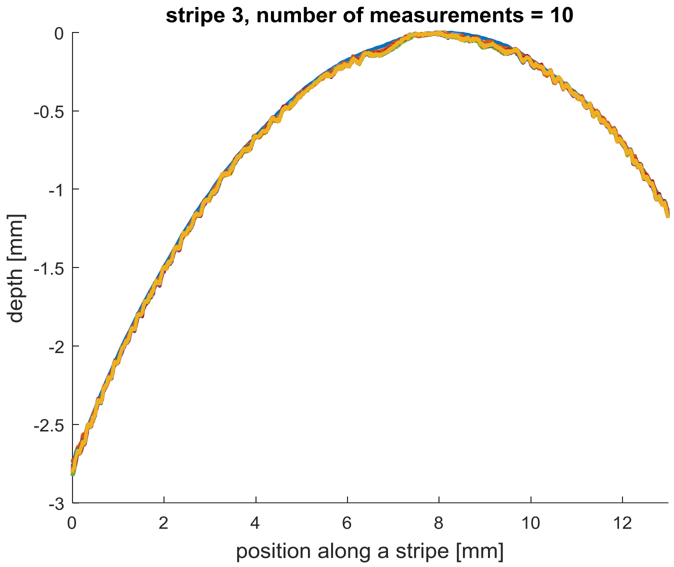

Figure 5-20: Depth along the third projected stripe on the cylinder was measured ten times in a row. All ten measurements all plotted in the same graph in ten different colors. The standard deviation of these ten measurements averaged over all the pixels on one stripe is 8.3 microns.

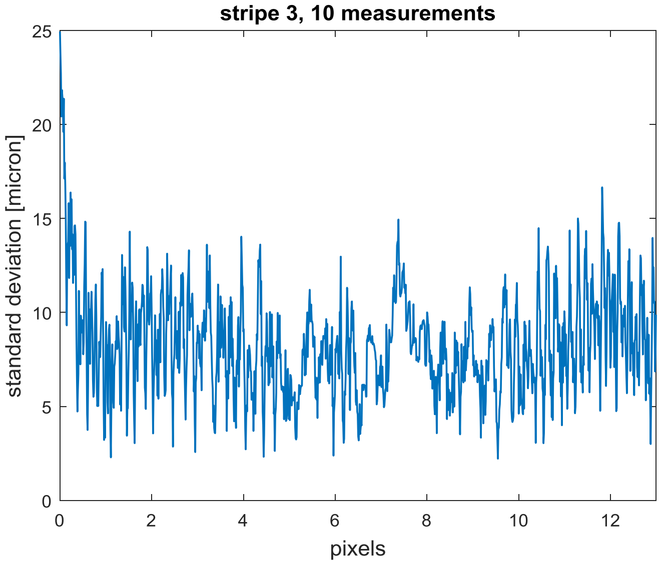

Figure 5-21: The standard deviation of ten subsequent measurements of the cylinder along the third projected stripe.

5.8 Summary

A 3D shape measurement technique was introduced in this chapter. We used the dispersive lens system described in Chapter 4 along with active shape from defocus technique to measure depth. A number of parallel stripes were projected onto the object at two different wavelengths (red and green), one wavelength at the time. An image was captured under each projection. The degree at which each stripe is defocused in the captured images contains information about the depth of the object. Due to dispersion of the camera's lens system, changing the wavelength of projection is equivalent of changing the focus setting of the camera. Therefore, we were able to develop a 3D shape measurement technique without mechanically moving any part.

We measured two different parts, one with a wedge shape and one with a cylindrical shape, with the introduced technique. The measurement results along three projected stripes were reported in this chapter. The repeatability of measured values averaged over each stripe was 10.9, 11.4 and 13 microns for the wedge sample along the first, second and third stripe, respectively. The repeatability of measured values averaged over each stripe was 13.1, 8.6 and 8.3 microns for the cylindrical sample along the first, second and third stripe, respectively.

CHAPTER 6 : CONCLUSION

A conventional camera captures two dimensional intensity map of a scene. By introducing chromatic aberration in the camera lens, we built a camera that adds a third dimension to the captured image. This third dimension can be either spectral or depth information of the scene. In other words, our camera can be used as a spectral imager or a depth measurement tool. If the additional third dimension is spectral information, our camera functions as a spectral imager and measures the spectral content of a flat object. If the third dimension is depth information, our camera measures the depth map of a 3D scene. These two functionalities are the subjects of Chapter 4 and Chapter 5 of this dissertation, respectively.

A vital component of our camera is its highly chromatic lens sytem. The ideal lens system for our purpose should be highly chromatic and yet it should still form good-quality images across the camera's field of view. We would like the lens system to disperse and spread the spectral information of the object over the camera's focal volume and focus each wavelength at a distinctive image location. At the same time, we would like the image to be perfectly in-focus for all wavelengths on their corresponding image locations. Section 4.1 describes the design procedure for this lens system.

The second component of the camera is a computational unit that analyses images captured by the dispersive lens system and calculates the spectrum or depth of the object from those images. When the camera is used as a spectral imager, the computational unit performs spectrum from focus algorithm. A sequence of images of the object are captured by placing the imaging sensor at different distances from the lens system. The computational unit searches for the locations of focused image for all points across the field of view. Each location of focused image corresponds to a wavelength in the spectrum of the object. When the camera is used as a depth measurement tool, the computational unit implements active shape from defocus technique. A projector projects a set of parallel stripe on the object. The computational unit calculates the spread of these stripes on captured images and uses that to compute the 3D depth of the object.

There is one major difference between the spectral imaging and depth measurement functionalities of our camera. When used as a spectral imager, a single point on the object can have multiple spectral lines and even a continuous spectrum but when used as a depth measurement tool, a single point on the object has only one depth value. This difference impacts the choice of algorithm that is implemented by the computational unit. This is the reason why the computational unit used spectrum from focus algorithm for the spectral imager in Chapter 4. Having multiple spectral lines would result in multiple peaks in focus measure function. Each peak corresponds to a wavelength. The effect is more complex if the computational unit uses spectrum from defocus and tries to measure the blur caused by multiple spectral lines at a specific image location. This limitation does not exist for depth measurement functionality and the computational unit uses active shape from defocus algorithm for depth measurement as described in Chapter 5.

The spectral and spatial resolutions of our SI technique are can be improved simultaneously. This is in contrast with conventional SI techniques where there is a trade-off between these two resolutions. Spectral resolution of our spectral imager depends on the amount of chromatic aberration produced by the lens system. The spatial resolution, on the other hand, is determined by the spatial resolution of the lens system.

The chromatic aberration of the lens system separates the spectral content of the object and images different wavelengths of the object at different locations. The larger the chromatic aberration, the more separate are the wavelengths and the higher is the spectral resolution of the spectral imager. The diffraction-limited spectral resolution comes from the fact that a spectral line in the object is imaged not to a point but to an axial intensity distribution. The width of this distribution is the theoretical limit for the spectral resolution of our spectral imaging technique and is a function of wavelength, magnification and numerical aperture of the lens system (equation (4-5)). This resolution is about 2 nm for our designed lens system. 2 nm is the theoretical limit that can be achieved. However, our 3-piece all-spherical lens system does not have a diffraction-limited performance and the actual spectral resolution is higher than the theoretical limit. The actual working resolution was calculated to be 4 nm for our spectral imager when there is no noise. The way that we calculated this resolution was that we introduced two spectral lines in the spectrum of the object and made the two spectral lines closer and closer until they were not resolved by the spectral imager anymore.

The actual resolution depends on the level of noise present in the system as well. Different levels of noise were introduced into the system to see what is the maximum level of noise until two spectral lines that are 4 nm apart cannot be resolved by the system anymore. We added both irradiance-dependent and irradiance-independent noises to captured images. The spectral imager maintains the 4nm spectral resolution for noise levels with variance values up to 0.0032.

The spatial resolution of our SI system is the spatial resolution of the lens system. For our 3-piece all-spherical lens system, the spatial resolution is limited by the spot size of the lens system rather than the pixel size of the imaging sensor. The spatial resolution changes depending on what magnification is the system being used at. The maximum RMS spot size across the field of view is 39 microns for $M = -1$ and is 46 microns for $M = -0.5$ configurations.

When the camera is used as a depth measurement tool, we project a pattern of parallel stripes onto the object at two different wavelengths and capture an image at each wavelength. Each projection pattern gets defocused as a function of object's depth. Additionally, due to dispersion, the lens system has different focal lengths at these two projection wavelengths and the amount of defocus varies between the two captured images. Effectively, by taking advantage of the dispersion of the lens system, we change the focal length of the camera by changing the wavelength of the illumination instead of moving the object or any other part of the imaging system. The amount of defocus in the two captured images is used to calculate the depth map of the object.

Unlike stereo-based approaches, our depth measurement technique uses images captured by a single camera but at different wavelengths of illumination to calculate the depth of the object. Therefore, our technique does not have to solve the issue of correspondence between two images as in stereo. In our introduced depth measurement technique, we make use of the dispersion of the camera and change the focus setting of the camera by changing the wavelength of the projection without mechanically moving any component. Thus, our technique does not involve any mechanical movement. Additionally, the projector and the camera in our technique share the same optical axis. Hence, they do not suffer from occlusion and shadowing problems like other active depth measurement techniques such as triangulation or structured-light based approaches where there is an angle between the projector and the camera.

We measured two different parts, one with a wedge shape and one with a cylindrical shape, with the introduced technique. The repeatability of measured values averaged over each stripe was 10.9, 11.4 and 13 microns for the wedge sample on the first, second and third stripe, respectively. The repeatability of measured values averaged over each stripe was 13.1, 8.6 and 8.3 microns for the cylindrical sample on the first, second and third stripe, respectively.

REFERENCES

1. Goetz, A.F., *Measuring the Earth from Above: 30 Years(and Counting) of Hyperspectral Imaging.* Photonics Spectra, 2011. **45**(6): p. 42-47.
2. Mehl, P.M., et al., *Development of hyperspectral imaging technique for the detection of apple surface defects and contaminations.* Journal of Food Engineering, 2004. **61**(1): p. 67-81.
3. Vasefi, F., et al., *Transillumination hyperspectral imaging for histopathological examination of excised tissue.* Journal of biomedical optics, 2011. **16**(8): p. 086014-086014-11.
4. Deck, L. and P. De Groot, *High-speed noncontact profiler based on scanning white-light interferometry.* Applied optics, 1994. **33**(31): p. 7334-7338.
5. Harding, K., *Handbook of optical dimensional metrology*. 2013: CRC Press.
6. Gorthi, S.S. and P. Rastogi, *Fringe projection techniques: whither we are?* Optics and lasers in engineering, 2010. **48**(IMAC-REVIEW-2009-001): p. 133-140.
7. Hartley, R.I. and P. Sturm, *Triangulation.* Computer vision and image understanding, 1997. **68**(2): p. 146-157.
8. Cui, Y., et al. *3D shape scanning with a time-of-flight camera*. in *Computer Vision and Pattern Recognition (CVPR), 2010 IEEE Conference on*. 2010. IEEE.
9. Seitz, S.M., et al. *A comparison and evaluation of multi-view stereo reconstruction algorithms*. in *Computer vision and pattern recognition, 2006 IEEE Computer Society Conference on*. 2006. IEEE.
10. Jamshidi, J., et al., *Manufacturing and assembly automation by integrated metrology systems for aircraft wing fabrication.* Proceedings of the Institution of Mechanical Engineers, Part B: Journal of Engineering Manufacture, 2010. **224**(1): p. 25-36.
11. Molesini, G., et al., *Focus-wavelength encoded optical profilometer.* Optics communications, 1984. **49**(4): p. 229-233.
12. Browne, M., O. Akinyemi, and A. Boyde, *Confocal surface profiling utilizing chromatic aberration.* Scanning, 1992. **14**(3): p. 145-153.
13. Tiziani, H.J. and H.-M. Uhde, *Three-dimensional image sensing by chromatic confocal microscopy.* Applied optics, 1994. **33**(10): p. 1838-1843.
14. Cha, S., et al., *Nontranslational three-dimensional profilometry by chromatic confocal microscopy with dynamically configurable micromirror scanning.* Applied optics, 2000. **39**(16): p. 2605-2613.
15. Pawley, J. and B.R. Masters, *Handbook of biological confocal microscopy.* Optical Engineering, 1996. **35**(9): p. 2765-2766.
16. Minsky, M., *Confocal Patent focal Scanning Microscope.* US patent, serial, 1957(3,013,467).
17. Pertuz, S., D. Puig, and M. Angel Garcia, *Analysis of focus measure operators for shape-from-focus.* Pattern Recognition, 2012.

18. Nair, H.N. and C.V. Stewart. *Robust focus ranging*. in *Computer Vision and Pattern Recognition, 1992. Proceedings CVPR'92., 1992 IEEE Computer Society Conference on*. 1992. IEEE.
19. Subbarao, M., T. Choi, and A. Nikzad, *Focusing techniques.* Machine Vision Applications Architectures, and Systems Integration (Proceedings of SPIE): 17-18 November 1992; Boston, 1992: p. 163-174.
20. Chern, N.N.K., P.A. Neow, and M.H. Ang. *Practical issues in pixel-based autofocusing for machine vision*. in *Robotics and Automation, 2001. Proceedings 2001 ICRA. IEEE International Conference on*. 2001. IEEE.
21. Helmli, F.S. and S. Scherer. *Adaptive shape from focus with an error estimation in light microscopy*. in *Image and Signal Processing and Analysis, 2001. ISPA 2001. Proceedings of the 2nd International Symposium on*. 2001. IEEE.
22. Nayar, S.K. and Y. Nakagawa, *Shape from focus.* Pattern Analysis and Machine Intelligence, IEEE Transactions on, 1994. **16**(8): p. 824-831.
23. Sun, Y., S. Duthaler, and B.J. Nelson, *Autofocusing in computer microscopy: selecting the optimal focus algorithm.* Microscopy research and technique, 2004. **65**(3): p. 139-149.
24. Huang, W. and Z. Jing, *Evaluation of focus measures in multi-focus image fusion.* Pattern recognition letters, 2007. **28**(4): p. 493-500.
25. Thelen, A., et al., *Improvements in shape-from-focus for holographic reconstructions with regard to focus operators, neighborhood-size, and height value interpolation.* IEEE Transactions on Image Processing, 2009. **18**(1): p. 151-157.
26. Yang, G. and B.J. Nelson. *Wavelet-based autofocusing and unsupervised segmentation of microscopic images*. in *Intelligent Robots and Systems, 2003.(IROS 2003). Proceedings. 2003 IEEE/RSJ International Conference on*. 2003. IEEE.
27. Huang, J.-T., et al. *Robust measure of image focus in the wavelet domain*. in *Intelligent Signal Processing and Communication Systems, 2005. ISPACS 2005. Proceedings of 2005 International Symposium on*. 2005. IEEE.
28. Xie, H., W. Rong, and L. Sun. *Wavelet-based focus measure and 3-d surface reconstruction method for microscopy images*. in *Intelligent Robots and Systems, 2006 IEEE/RSJ International Conference on*. 2006. IEEE.
29. Pentland, A.P., *A new sense for depth of field.* Pattern Analysis and Machine Intelligence, IEEE Transactions on, 1987(4): p. 523-531.
30. Torreao, J.R. and J.L. Fernandes. *Single-image shape from defocus*. in *Computer Graphics and Image Processing, 2005. SIBGRAPI 2005. 18th Brazilian Symposium on*. 2005. IEEE.
31. Tai, Y.-W. and M.S. Brown. *Single image defocus map estimation using local contrast prior*. in *Image Processing (ICIP), 2009 16th IEEE International Conference on*. 2009. IEEE.
32. Zhuo, S. and T. Sim, *Defocus map estimation from a single image.* Pattern Recognition, 2011. **44**(9): p. 1852-1858.

33. Rioux, M. and F. Blais, *Compact three-dimensional camera for robotic applications.* JOSA A, 1986. **3**(9): p. 1518-1521.
34. Pentland, A., et al., *Simple range cameras based on focal error.* JOSA A, 1994. **11**(11): p. 2925-2934.
35. Watanabe, M., S.K. Nayar, and M.N. Noguchi. *Real-time computation of depth from defocus*. in *Photonics East'95*. 1996. International Society for Optics and Photonics.
36. Ghita, O., P.F. Whelan, and J. Mallon, *Computational approach for depth from defocus.* Journal of Electronic Imaging, 2005. **14**(2): p. 023021-023021-8.
37. Zhang, L. and S. Nayar. *Projection defocus analysis for scene capture and image display*. in *ACM Transactions on Graphics (TOG)*. 2006. ACM.
38. Lertrusdachakul, I., Y.D. Fougerolle, and O. Laligant. *A novel 3D reconstruction approach by dynamic (de) focused light*. in *IS&T/SPIE Electronic Imaging*. 2010. International Society for Optics and Photonics.
39. Lertrusdachakul, I., Y.D. Fougerolle, and O. Laligant, *Dynamic (de) focused projection for three-dimensional reconstruction.* Optical Engineering, 2011. **50**(11): p. 113201-113201-11.
40. Eismann, M.T. *Hyperspectral remote sensing*. 2012. SPIE Bellingham.
41. ElMasry, G., et al., *Principles and applications of hyperspectral imaging in quality evaluation of agro-food products: a review.* Critical Reviews in Food Science and Nutrition, 2012. **52**(11): p. 999-1023.
42. Lu, G. and B. Fei, *Medical hyperspectral imaging: a review.* Journal of biomedical optics, 2014. **19**(1): p. 010901-010901.
43. Kuula, J., et al. *Using VIS/NIR and IR spectral cameras for detecting and separating crime scene details*. in *SPIE Defense, Security, and Sensing*. 2012. International Society for Optics and Photonics.
44. Liang, H., *Advances in multispectral and hyperspectral imaging for archaeology and art conservation.* Applied Physics A, 2012. **106**(2): p. 309-323.
45. Feng, Y.-Z. and D.-W. Sun, *Application of hyperspectral imaging in food safety inspection and control: a review.* Critical Reviews in Food Science and Nutrition, 2012. **52**(11): p. 1039-1058.
46. Qin, J., et al., *Detection of citrus canker using hyperspectral reflectance imaging with spectral information divergence.* Journal of food engineering, 2009. **93**(2): p. 183-191.
47. Li, J., X. Rao, and Y. Ying, *Detection of common defects on oranges using hyperspectral reflectance imaging.* Computers and Electronics in Agriculture, 2011. **78**(1): p. 38-48.
48. Tallada, J.G., M. Nagata, and T. Kobayashi, *Non-destructive estimation of firmness of strawberries (Fragaria× ananassa Duch.) using NIR hyperspectral imaging.* Environmental Control in Biology, 2006. **44**(4): p. 245-255.
49. ElMasry, G., et al., *Meat quality evaluation by hyperspectral imaging technique: an overview.* Critical reviews in food science and nutrition, 2012. **52**(8): p. 689-711.

50. Park, B., et al., *Performance of hyperspectral imaging system for poultry surface fecal contaminant detection.* Journal of Food Engineering, 2006. **75**(3): p. 340-348.
51. Benavides, J.M., et al., *Multispectral digital colposcopy for in vivo detection of cervical cancer.* Optics Express, 2003. **11**(10): p. 1223-1236.
52. Siddiqi, A.M., et al., *Use of hyperspectral imaging to distinguish normal, precancerous, and cancerous cells.* Cancer Cytopathology, 2008. **114**(1): p. 13-21.
53. Hattery, D., et al. *Hyperspectral imaging of Kaposi's Sarcoma for disease assessment and treatment monitoring*. in *Applied Imagery Pattern Recognition Workshop, 2002. Proceedings. 31st*. 2002. IEEE.
54. Dicker, D.T., et al., *Differentiation of normal skin and melanoma using high resolution hyperspectral imaging.* Cancer biology & therapy, 2006. **5**(8): p. 1033-1038.
55. Renkoski, T.E., K.D. Hatch, and U. Utzinger, *Wide-field spectral imaging of human ovary autofluorescence and oncologic diagnosis via previously collected probe data.* Journal of biomedical optics, 2012. **17**(3): p. 0360031-03600313.
56. Argov, S., et al., *Diagnostic potential of Fourier-transform infrared microspectroscopy and advanced computational methods in colon cancer patients.* Journal of biomedical optics, 2002. **7**(2): p. 248-254.
57. Masood, K. and N. Rajpoot. *Texture based classification of hyperspectral colon biopsy samples using CLBP*. in *Biomedical Imaging: From Nano to Macro, 2009. ISBI'09. IEEE International Symposium on*. 2009. IEEE.
58. Roblyer, D., et al., *Multispectral optical imaging device for in vivo detection of oral neoplasia.* Journal of biomedical optics, 2008. **13**(2): p. 024019-024019-11.
59. Pierce, M.C., et al., *Accuracy of in vivo multimodal optical imaging for detection of oral neoplasia.* Cancer Prevention Research, 2012. **5**(6): p. 801-809.
60. Zuzak, K.J., et al., *Intraoperative bile duct visualization using near-infrared hyperspectral video imaging.* The American Journal of Surgery, 2008. **195**(4): p. 491-497.
61. Holzer, M.S., et al., *Assessment of renal oxygenation during partial nephrectomy using hyperspectral imaging.* The Journal of urology, 2011. **186**(2): p. 400-404.
62. Akbari, H., et al. *Blood vessel detection and artery-vein differentiation using hyperspectral imaging*. in *Engineering in Medicine and Biology Society, 2009. EMBC 2009. Annual International Conference of the IEEE*. 2009. IEEE.
63. Sellar, R.G. and G.D. Boreman, *Classification of imaging spectrometers for remote sensing applications.* Optical Engineering, 2005. **44**(1): p. 013602-013602-3.
64. Brauers, J., N. Schulte, and T. Aach, *Multispectral filter-wheel cameras: Geometric distortion model and compensation algorithms.* IEEE Transactions on Image Processing, 2008. **17**(12): p. 2368-2380.
65. Gat, N. *Imaging spectroscopy using tunable filters: a review*. in *AeroSense 2000*. 2000. International Society for Optics and Photonics.

66. Sun, D.-W., *Hyperspectral imaging for food quality analysis and control*. 2010: Elsevier.
67. Randeberg, L.L., et al. *Hyperspectral imaging of bruised skin*. in *Biomedical Optics 2006*. 2006. International Society for Optics and Photonics.
68. Larsen, E.L., et al., *Hyperspectral imaging of atherosclerotic plaques in vitro.* Journal of biomedical optics, 2011. **16**(2): p. 026011-026011-11.
69. Kester, R.T., et al., *Real-time snapshot hyperspectral imaging endoscope.* Journal of biomedical optics, 2011. **16**(5): p. 056005-056005-12.
70. Lawrence, K.C., et al., *Calibration of a pushbroom hyperspectral imaging system for agricultural inspection.* TRANSACTIONS-AMERICAN SOCIETY OF AGRICULTURAL ENGINEERS, 2003. **46**(2): p. 513-522.
71. Akbari, H., et al., *Cancer detection using infrared hyperspectral imaging.* Cancer science, 2011. **102**(4): p. 852-857.
72. Aikio, M. and V. Tutkimuskeskus, *Hyperspectral prism-grating-prism imaging spectrograph*. 2001: Technical Research Centre of Finland.
73. Colarusso, P., et al., *Infrared spectroscopic imaging: from planetary to cellular systems.* Applied Spectroscopy, 1998. **52**(3): p. 106A-120A.
74. Schumann, L.W. and T.S. Lomheim. *Infrared hyperspectral imaging Fourier transform and dispersive spectrometers: comparison of signal-to-noise-based performance*. in *International Symposium on Optical Science and Technology*. 2002. International Society for Optics and Photonics.
75. Mathews, S.A., *Design and fabrication of a low-cost, multispectral imaging system.* Applied optics, 2008. **47**(28): p. F71-F76.
76. Matsuoka, H., et al., *Single-cell viability assessment with a novel spectro-imaging system.* Journal of biotechnology, 2002. **94**(3): p. 299-308.
77. Bodkin, A., A. Sheinis, and A. Norton, *Hyperspectral imaging systems*. 2005, Google Patents.
78. Ford, B.K., et al., *Computed tomography-based spectral imaging for fluorescence microscopy.* Biophysical Journal, 2001. **80**(2): p. 986-993.
79. Hege, E.K., et al. *Hyperspectral imaging for astronomy and space surviellance*. in *Optical Science and Technology, SPIE's 48th Annual Meeting*. 2004. International Society for Optics and Photonics.
80. Johnson, W.R., D.W. Wilson, and G. Bearman, *Spatial-spectral modulating snapshot hyperspectral imager.* Applied optics, 2006. **45**(9): p. 1898-1908.
81. Johnson, W.R., et al., *Snapshot hyperspectral imaging in ophthalmology.* Journal of biomedical optics, 2007. **12**(1): p. 014036-014036-7.
82. Gehm, M., et al., *Single-shot compressive spectral imaging with a dual-disperser architecture.* Optics Express, 2007. **15**(21): p. 14013-14027.
83. Wagadarikar, A., et al., *Single disperser design for coded aperture snapshot spectral imaging.* Applied optics, 2008. **47**(10): p. B44-B51.
84. Arce, G.R., et al., *Compressive coded aperture spectral imaging: An introduction.* IEEE Signal Processing Magazine, 2014. **31**(1): p. 105-115.

85. Kester, R.T., N. Bedard, and T.S. Tkaczyk. *Image mapping spectrometry: a novel hyperspectral platform for rapid snapshot imaging*. in *SPIE Defense, Security, and Sensing*. 2011. International Society for Optics and Photonics.
86. Smith, W.J., *Modern lens design*. Vol. 2. 2005: McGraw-Hill New York.
87. *Flea3 1.3 MP Mono USB3 Vision (e2v EV76C560)*. Available from: https://www.ptgrey.com/flea3-13-mp-mono-usb3-vision-e2v-ev76c560-camera.
88. Novotny, L. and B. Hecht, *Principles of nano-optics*. 2012: Cambridge university press.
89. Cryan, C. and R. Strack, *Fiber optic faceplate*. 2002, Google Patents.
90. Xie, H., W. Rong, and L. Sun, *Construction and evaluation of a wavelet-based focus measure for microscopy imaging.* Microscopy research and technique, 2007. **70**(11): p. 987-995.
91. Watanabe, M. and S.K. Nayar. *Telecentric optics for computational vision*. in *European Conference on Computer Vision*. 1996. Springer.
92. Liu, C., et al., *Automatic estimation and removal of noise from a single image.* IEEE transactions on pattern analysis and machine intelligence, 2008. **30**(2): p. 299-314.
93. *SHOWWX Laser Pico Projector User Guide*. Available from: http://www.microvision.com/wp-content/uploads/2014/08/SHOWWX-User-Guide.pdf.
94. Saakov, V.S., et al., *Derivative spectrophotometry and electron spin resonance (ESR) spectroscopy for ecological and biological questions*. 2012: Springer Science & Business Media.
95. Pieper, R.J., J. Park, and T.-C. Poon, *Resolution-dependent depth of focus for an incoherent imaging system.* Applied optics, 1988. **27**(10): p. 2040-2047.
96. Girod, B. and S. Scherock. *Depth from defocus of structured light*. in *1989 Advances in Intelligent Robotics Systems Conference*. 1990. International Society for Optics and Photonics.